THE GEOLOGICAL SOCIETY OF AMERICA®

Miocene ice sheet dynamics and sediment deposition in the central Ross Sea, Antarctica

Robert McKay[1,†], Jay Cockrell[1,2], Amelia E. Shevenell[3], Jan Sverre Laberg[4], Julianne Burns[1], Molly Patterson[5], Sunghan Kim[6], Tim Naish[1], David Harwood[7], Richard Levy[1,8], James Marschalek[9], Tina van de Flierdt[9], Saki Ishino[10], Benjamin Keisling[11], Isabel Moreno Cordeiro de Sousa[12], Giuseppe Cortese[8], Francesca Sangiorgi[13], R. Mark Leckie[14], Justin Dodd[15], Bella Duncan[1], Lara F. Pérez[16], Brian W. Romans[17], Sookwan Kim[18], Samantha Bombard[14], Imogen Browne[3], Tim van Peer[19], Osamu Seki[20], Florence Colleoni[21], Denise Kulhanek[5,22], Laura De Santis[21], and the IODP Expedition 374 Science Team[23]

[1]*Antarctic Research Centre, Victoria University of Wellington, Wellington 6012, New Zealand*
[2]*Materials Management Division, Michigan Department of Environment, Great Lakes, and Energy, Lansing, Michigan 48909, USA*
[3]*College of Marine Science, University of South Florida, St. Petersburg, Florida 33701, USA*
[4]*Department of Geosciences, UiT The Arctic University of Norway, N-9037 Tromsø, Norway*
[5]*Department of Earth Sciences, Binghamton University, State University of New York, Binghamton, New York 13902, USA*
[6]*Korea Polar Research Institute, Incheon, Republic of Korea*
[7]*Department of Earth and Atmospheric Sciences, University of Nebraska–Lincoln, Lincoln, Nebraska 68588, USA*
[8]*GNS Science, Lower Hutt 5011, New Zealand*
[9]*Department of Earth Science and Engineering, Imperial College London, London SW7 2AZ, UK*
[10]*Geological Survey of Japan, Tokyo 100-8921, Japan*
[11]*Institute for Geophysics, University of Texas at Austin, Austin, Texas 78758, USA*
[12]*Instituto de Geociencias, Universidade de Brasília, Brasília 70.910-900, Brazil*
[13]*Department of Earth Sciences, Utrecht University, 3584 CS Utrecht, The Netherlands*
[14]*Department of Earth, Geographic, and Climate Sciences, University of Massachusetts, Amherst, Massachusetts 01003, USA*
[15]*Department of Earth, Atmosphere and Environment, Northern Illinois University, Dekalb, Illinois 60115, USA*
[16]*Geological Survey of Denmark and Greenland (GEUS), 1350 København, Denmark*
[17]*Department of Geosciences, Virginia Tech, Blacksburg, Virginia 24061, USA*
[18]*Korea Institute of Ocean Science and Technology, Busan, Republic of Korea*
[19]*School of Geography, Geology and the Environment, University of Leicester, Leicester LE1 7RH, UK*
[20]*Institute of Low Temperature Science, Hokkaido University, Sapporo, Hokkaido 0600819, Japan*
[21]*National Institute of Oceanography and Applied Geophysics (OGS), Trieste, 34010 Sgonico TS, Italy*
[22]*Institute of Geosciences, Christian-Albrechts-University of Kiel, 24118 Kiel, Germany*
[23]*International Ocean Discovery Program, Texas A&M University, College Station, Texas 77845, USA*

ABSTRACT

Drill cores from the Antarctic continental shelf are essential for directly constraining changes in past Antarctic Ice Sheet extent. Here, we provide a sedimentary facies analysis of drill cores from International Ocean Discovery Program (IODP) Site U1521 in the Ross Sea, which reveals a unique, detailed snapshot of Antarctic Ice Sheet evolution between ca. 18 Ma and 13 Ma. We identify distinct depositional packages, each of which contains facies successions that are reflective of past baseline shifts in the presence or absence of marine-terminating ice sheets on the outermost Ross Sea continental shelf. The oldest depositional package (>18 Ma) contains massive diamictites stacked through aggradation and deposited in a deep, actively subsiding basin that restricted marine ice sheet expansion on the outer continental shelf. A slowdown in tectonic subsidence after 17.8 Ma led to the deposition of progradational massive diamictites with thin mudstone beds/laminae, as several large marine-based ice sheet advances expanded onto the mid- to outer continental shelf between 17.8 Ma and 17.4 Ma. Between 17.2 Ma and 15.95 Ma, packages of interbedded diamictite and diatom-rich mudstone were deposited during a phase of highly variable Antarctic Ice Sheet extent and volume. This included periods of Antarctic Ice Sheet advance near the outer shelf during the early Miocene Climate Optimum (MCO)—despite this being a well-known period of peak global warmth between ca. 17.0 Ma and 14.6 Ma. Conversely, there were periods of peak warmth within the MCO during which diatom-rich mudstones with little to no ice-rafted debris were deposited, which indicates that the Antarctic Ice Sheet was greatly reduced in extent and had retreated to a smaller terrestrial-terminating ice sheet, most notably between 16.3 Ma and 15.95 Ma. Post-14.2 Ma, diamictites and diatomites contain unambiguous evidence of subglacial shearing in the core and provide

Robert McKay https://orcid.org/0000-0002-5602-6985
[†]robert.mckay@vuw.ac.nz

GSA Bulletin;
published online 9 October 2024

https://doi.org/10.1130/B37613.1.

the first direct, well-dated evidence of highly erosive marine ice sheets on the outermost continental shelf during the onset of the Middle Miocene Climate Transition (MMCT; 14.2–13.6 Ma). Although global climate forcings and feedbacks influenced Antarctic Ice Sheet advances and retreats during the MCO and MMCT, we propose that this response was nonlinear and heavily influenced by regional feedbacks related to the shoaling of the continental shelf due to reduced subsidence, sediment infilling, and local sea-level changes that directly influenced oceanic influences on melting at the Antarctic Ice Sheet margin. Although intervals of diatom-rich muds and diatomite indicating open-marine interglacial conditions still occurred during (and following) the MMCT, repeated advances of marine-based ice sheets since that time have resulted in widespread erosion and overdeepening in the inner Ross Sea, which has greatly enhanced sensitivity to marine ice sheet instability since 14.2 Ma.

INTRODUCTION

Deep-sea geochemical and modeling studies indicate that during the Oligocene (33.9–23 Ma) and early to middle Miocene (23–11.6 Ma), Antarctica's ice sheets expanded and contracted (e.g., Zachos et al., 1997, 2001; Pekar and DeConto, 2006; Pekar et al., 2006; Pälike et al., 2006). These variations are proposed to have been driven by fluctuating atmospheric pCO_2 levels and/or tectonically driven changes in poleward heat and moisture transport, which were paced by changes in Earth's orbital configuration (e.g., DeConto and Pollard, 2003; Shevenell et al., 2004, 2008; CenCO$_2$PIP Consortium, 2023). The Antarctic Ice Sheet advances are inferred to reflect eustatic sea-level variances of 40–65 m (Flower and Kennett, 1994; Zachos et al., 2001; Kominz et al., 2008; John et al., 2011; Miller et al., 2020). However, most of this ice sheet history is inferred from benthic foraminiferal $\delta^{18}O$ records, which are a measure of global ice volume and deep-sea temperature, or far-field sea-level records that contain uncertainties related to tectonic processes. To address these uncertainties, drill-core evidence from Antarctica's continental margin and the Southern Ocean provide direct evidence that Antarctica's marine-terminating glaciers have expanded and retreated at orbital time scales since the Eocene (56–33.9 Ma) and are likely the origin of these global sea-level variations (Barrett, 1989; Hambrey et al., 1992; Zachos et al., 1992; Naish et al., 2001a; McKay et al., 2012a; Escutia et al., 2014; Galeotti et al., 2016; Carter et al., 2017; Gulick, Shevenell, et al., 2017; Levy et al., 2019). However, the locations of many of these previous studies are at the periphery of the modern East Antarctic Ice Sheet, either in mountain outcrops or inner continental shelf records. This means it is often difficult to determine whether those records represent grounded continental-scale ice sheet expansion to the outermost continental shelf, or result from smaller-scale advances of the inland East Antarctic Ice Sheet to its coastal margin (Fig. 1). To elucidate major differences in the extent of past ice sheet expansion, direct evidence of ice sheet grounding events from outer continental shelf drill cores is needed to constrain periods of maximum continental-scale Antarctic Ice Sheet advance and identify the Antarctic ice volume contribution to the far-field sea-level and deep-sea $\delta^{18}O$ records.

Throughout the Oligocene, Antarctic Ice Sheet expansions are thought to have been largely terrestrial and continent-wide (Wilson and Luyendyk, 2009; Naish et al., 2022). However, rifting, subsidence, and sediment deposition associated with the West Antarctic Rift System, coupled with an overriding erosive ice sheet, resulted in much of the sub-ice topography of the present-day West Antarctic Ice Sheet, which now lies largely below sea level (Sorlien et al., 2007; Wilson and Luyendyk, 2009; Wilson et al., 2013; Colleoni et al., 2018; Paxman et al., 2019, 2020). In deep-sea records, the Oligocene–Miocene transition (ca. 23.3–22.9 Ma) is characterized by a 0.6‰ increase in benthic foraminiferal $\delta^{18}O$ (Miller et al., 1991; Wright et al., 1992; Zachos et al., 1997; Mudelsee et al., 2014). In the Ross Sea, this transition is associated with an East Antarctic Ice Sheet advance on the inner shelf (Naish et al., 2001a, 2022; Duncan et al., 2022). Other Antarctic margin drill cores and marine geophysical records suggest that Antarctic Ice Sheet expansions into the marine margins of the Ross Sea occurred more frequently after the Oligocene–Miocene transition (Levy et al., 2019; Marschalek et al., 2021).

Widespread glacial retreat is proposed for the Miocene Climate Optimum (MCO; ca. 17.0–14.6 Ma), when global temperatures were

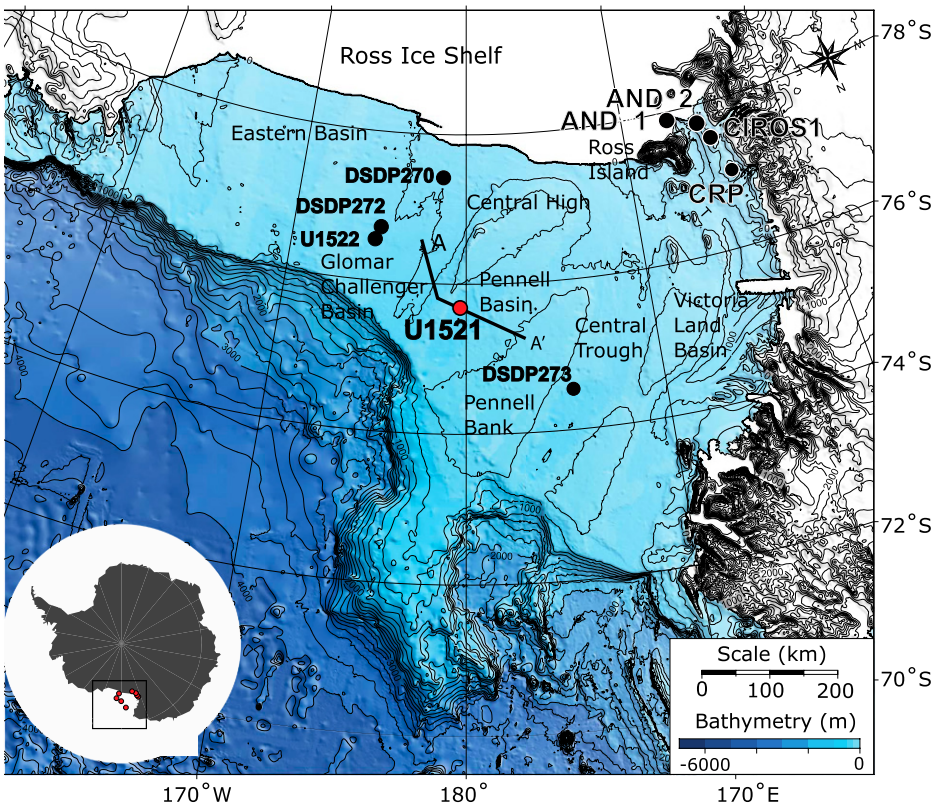

Figure 1. Location map of the central Ross Sea, Antarctica, study region and drill site locations (black dots) discussed in the text; Site U1521 (red dot on large map) was the primary site investigated in this project. Line A–A′ indicates the seismic profile shown in Figure 3. Figure was adapted from McKay et al. (2019). Bathymetry is from the International Bathymetric Chart of the Southern Ocean (Arndt et al., 2013). AND—Antarctic Geological Drilling; CIROS—Cenozoic Investigation in the Western Ross Sea; CRP—Cape Roberts Project; DSDP—Deep Sea Drilling Project.

~7–8 °C warmer than at present (Flower and Kennett, 1994; Shevenell et al., 2004, 2008; Lewis et al., 2007; You et al., 2009; Warny et al., 2009; Feakins et al., 2012; Levy et al., 2016; Sangiorgi et al., 2018). Carbon cycle feedbacks were proposed to have influenced this elevated global warmth, as atmospheric pCO_2 concentrations are thought to have ranged from 400 ppm to 833 ppm (Greenop et al., 2014; Sosdian et al., 2018; Ji et al., 2018; Cui et al., 2020; Steinthorsdottir et al., 2021; Rae et al., 2021; $CenCO_2PIP$ Consortium, 2023; Fig. 2). Far-field sea-level records show between ~40 m and 60 m of sea level variability before and during the MCO, and although larger-than-present ice sheets prior to the MCO do not require complete loss of the Antarctic Ice Sheet, the retreat of the East Antarctic Ice Sheet to small interior ice sheets is implied (John et al., 2011; Miller et al., 2020; Marschalek et al., 2021). Indeed, stratigraphic records from ANDRILL (Antarctic Geological Drilling) Site AND-2A and the Transantarctic Mountains, as well as consideration of dynamically modeled ice sheet experiments, suggest that although orbitally paced retreat of a terrestrial Antarctic Ice Sheet occurred, significant terrestrial ice remained (~20–30 m sea-level equivalent) during the MCO (Lewis et al., 2007; Passchier et al., 2011; Levy et al., 2016; Lewis and Ashworth, 2016; Gasson et al., 2016; Halberstadt et al., 2021; Chorley et al., 2022). However, whether or not periods of marine-terminating ice sheet advance into the outer Ross Sea occurred during glacial periods of the MCO is currently unknown.

The warm MCO was immediately followed by the Middle Miocene Climate Transition (MMCT, ca. 14.6–13.8 Ma), which was characterized by an ~1‰ increase in benthic foraminiferal $\delta^{18}O$ and an ~2–6 °C cooling in the Southern Ocean (Flower and Kennett, 1994; Shevenell et al., 2004, 2008; Miller et al., 2020). Well-dated drill cores of terrestrial fluvial and glacial sediments in the Friis Hills, Antarctica, reveal a progressive increase in the extent of orbitally paced East Antarctic Ice Sheet glaciations between 14.6 Ma and 13.8 Ma (Chorley et al., 2022), as well as increased aridity after 14.6 Ma at high elevations in the Transantarctic Mountains (Sugden and Denton, 2004; Lewis et al., 2008). From these inland records, ice expansion at the MMCT is proposed to have expanded across the entire Ross Sea continental shelf (Sugden and Denton, 2004), but this hypothesis has yet to be evaluated with well-dated Ross Sea drill cores from the outer continental shelf.

Here, we assess and expand on the broad interpretations from the aforementioned studies by developing a high-resolution depositional model for International Ocean Discovery Program (IODP) Site U1521—a location that ice sheet models and seismic stratigraphic studies indicate represents the maximum extent of a continental-scale Antarctic Ice Sheet during glacial intervals (Golledge et al., 2013; Colleoni et al., 2018; McKay et al., 2019). We evaluate the following hypotheses: (1) early Miocene tectonic subsidence restricted the growth of the early Miocene Antarctic Ice Sheet into the outer Ross Sea; (2) reduced subsidence after 17.8 Ma resulted in continental shelf progradation, and sediment infilling during expansive Antarctic Ice Sheet advances in the Ross Sea; (3) marine-terminating ice sheets existed in the Ross Sea during glacial periods of the MCO, but retreated inland during the peak warmth of the MCO; and (4) the MMCT saw the expansion of marine-based ice sheets to the outermost continental shelf of the Ross Sea, as has been proposed from inland studies and seismic data with limited age model control (Bart, 2003).

Our focus is on understanding the interplay of tectonics and sedimentation that led to the potential nonlinear response of the Antarctic Ice Sheet to climate forcing leading into and during the MCO, as well as the transition into the MMCT. Given that the global climate state of the MCO is increasingly relevant in the context of future emission scenarios, distinguishing the relative influences of climatic versus longer-term geological controls on Antarctic Ice Sheet evolution is important for helping to validate and calibrate processes in models used to project future ice sheet mass balance changes in a rapidly warming climate, similar to that observed in the MCO.

Background: Antarctic Continental Shelf Depositional Models Using Lithofacies Models and Other Criteria to Define Glacial Proximity

Numerous depositional models exist from the previous studies of Antarctic continental shelf drill cores, and these provide the framework for the facies succession methodology we describe in the Results and Discussion section (Naish et al., 2001b; Powell et al., 2001; McKay et al., 2009). In those studies, the base of a depositional glacial advance/retreat cycle is defined as the location within a facies succession that contains evidence of erosion and/or an abrupt facies dislocation due to either direct glacial overriding, or the most proximal deposition to a grounding line within an ice sheet advance-and-retreat cycle. Such deformational features, when assessed within a facies succession context, allow for identification of a glacial surface of erosion (GSE). If present, it forms the base of a depositional cycle (Fielding et al., 2000; Powell and Cooper, 2002; Naish et al., 2009). A GSE is commonly identified by a diamictite facies that includes a sharp basal contact overlying deformed and sheared facies that are also intermixed into the diamictite, which becomes increasingly massive and homogeneous in structure up-unit (Facies Dm-sh [sheared diamictite], Table 1; Fielding et al., 2000; McKay et al., 2009). Soft-sediment deformational features common in deforming glacier beds are also used to define GSEs and include a combination of highly sheared mudstone laminae or lenses, asymmetrical folding, dispersion tails or clast concentrations around larger clasts, sediment injection or diapir-like features, augen-shaped lenses of mudstone/diatomite intraclasts, and galaxy-like lens structures surrounding clasts that have formed from shearing or rotational processes (Boyce and Eyles, 2000).

Clasts plucked from underlying lithologies may also be incorporated into the base of the overlying sheared diamictite facies and are a key diagnostic feature near interpreted GSEs. Brittle deformational features, including low-angle reverse faulting and brecciation of the underlying facies, are also commonly identified in the sheared diamictite facies (McKay et al., 2012b). Such deformational features at the base of, and beneath, massive diamictite facies are consistent with previously established models of bed deformation resulting from overriding grounded ice (Boyce and Eyles, 2000; Boulton et al., 2001; McCarroll and Rijsdijk, 2003; McKay et al., 2012b; Evans and Benn, 2014).

Where poor core recovery precludes the identification of a GSE contact, multiple shearing/deformational features in the facies immediately preceding and following a core gap may indicate overriding of grounded ice at the site. However, deformational features and erosion surfaces not associated with GSEs can also occur in glacimarine settings proximal to the grounding line. Rotational features, flame structures, dewatering deformational features, and normal or reverse faulting may indicate rapid sediment deposition and/or deformation by slumping and mass flow processes (Mills, 1983; Powell and Molnia, 1989). Consequently, the identification of GSEs is based on multiple criteria, including stratigraphic context within the facies succession.

Massive diamictites (Dm) lacking sheared deformational features may also be associated with subglacial deposition; however, they are also commonly deposited in a glacimarine environment or open water with mass flow deposition (Powell and Molnia, 1989; Dowdeswell et al., 1994; Prothro et al., 2018). To address ambiguity, stratigraphic context can provide important insights into glacial proximity. Above the GSE, a typical facies succession of ice sheet retreat consists of an upward transition from

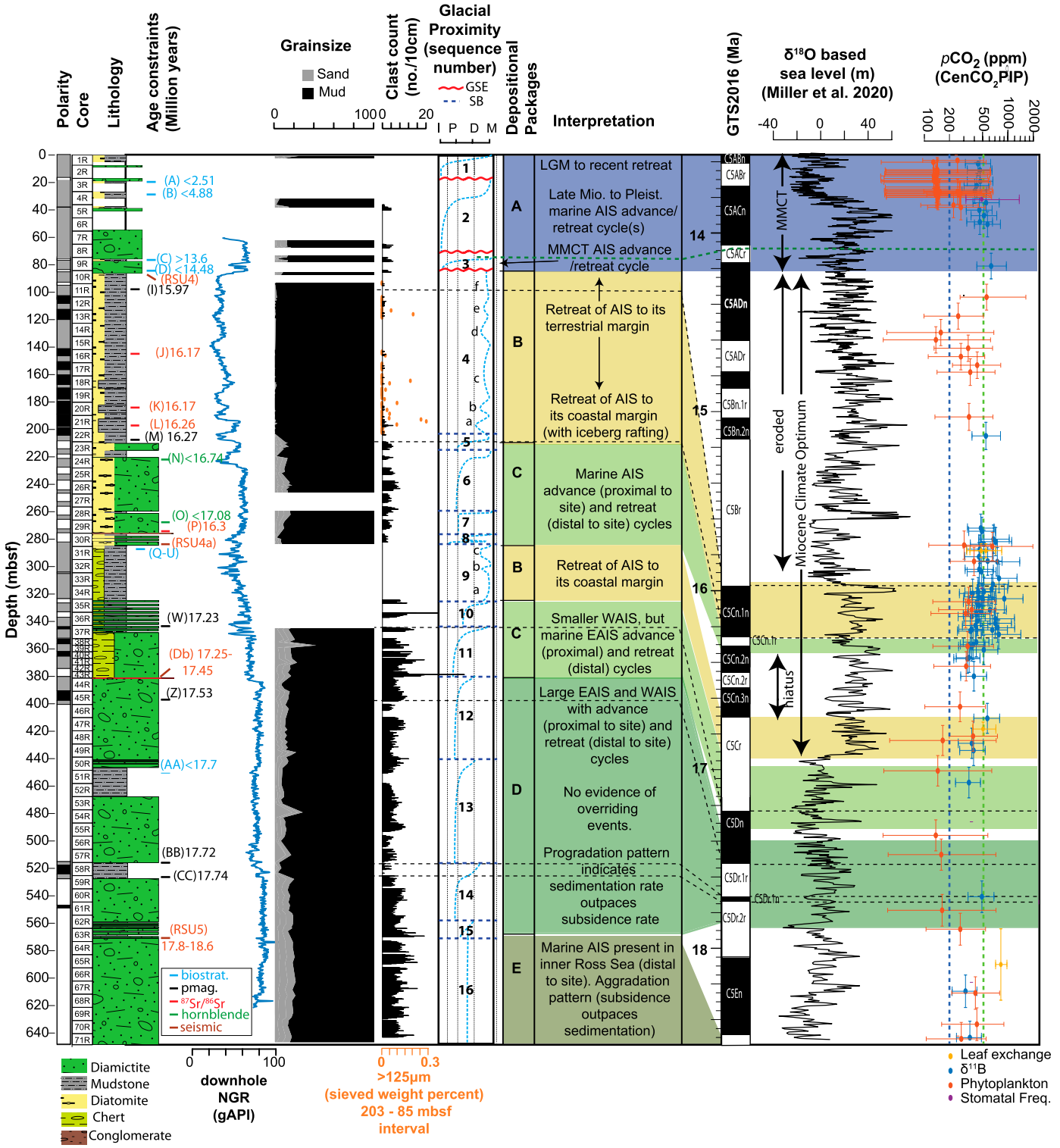

Figure 2. Summary of Site U1521 core properties showing, from left to right: Depth below seafloor; magnetostratigraphy (Marschalek et al., 2021); lithology; age constraints (Table 2); downhole log natural gamma radiation (NGR); grain size data (this study) and clast abundance in cut core face (Marschalek et al., 2021); seismic unconformities (Ross Sea unconformities, RSU; Pérez et al., 2022a); cycle numbers with glacial proximity curve (blue line; I—ice contact, P—ice proximal, D—ice distal, M—open marine), with non-glacially eroded sequence boundaries (SB; dark blue dotted line) and glacial surface of erosion sequence boundaries (GSE; red wavy line); depositional packages of Facies Successions A–E; interpretation; and correlation to the 2016 Geological Time Scale (GTS), sea-level curve of Miller et al. (2020), and proxy-based pCO_2 compilation of $CenCO_2PIP$ Consortium (2023). AIS—Antarctic Ice Sheet; EAIS—East Antarctic Ice Sheet; GSE—glacial surface of erosion; LGM—Last Glacial Maximum; Mio.—Miocene; MMCT—Middle Miocene Climate Transition; Pleist.—Pleistocene; WAIS—West Antarctic Ice Sheet.

TABLE 1. LITHOFACIES DESIGNATIONS WITH SIMPLIFIED AND PRELIMINARY PALEOENVIRONMENTAL INTERPRETATION

Facies code	Lithofacies name	Features	Preliminary paleoenvironmental interpretation	Equivalent facies in McKay et al. (2019)
Dm-sh	Sheared diamictite	Muddy/sandy diamictite (clast-rich to clast-poor). Biogenic silica content (0%–25%). Lower contacts typically display shearing zones, brecciation, faulting, and intermixing with underlying facies.	Subglacial deposition and deformation.	Facies 1
Dm	Massive diamictite	Muddy/sandy diamictite (clast-rich to clast-poor). Biogenic silica content (0%–25%). Fragmented carbonate shells are common. Mottled texture is suggestive of bioturbation present in some intervals. Pyrite and carbonate diagenesis are common in cores below 300 mbsf. May display soft sediment deformation and faulting.	Ice-proximal glacimarine deposits, rainout from floating ice, or subglacial deposition.	Facies 1
Ds	Stratified diamictite	Similar to Dm facies but with weak to well-defined stratification (centimeter- to meter-scale). Stratification is defined by color, matrix particle size, and/or clast concentration.	Glacimarine deposits.	Facies 2
Mm	Massive mudstone	Massive mudstones. Clast abundance varies from absent to dispersed (<1%). Diatom content is variable (0%–25%). Variable intensity of bioturbation.	Hemipelagic suspension settling from ice-proximal to ice-distal glacimarine/fluvial sediment.	Facies 3
Ms	Stratified mudstone	Stratified mudstones, as defined by color, matrix particle size, and/or clast concentration. Clasts abundance is absent to dispersed (<1%). Diatom content is variable (0%–25%). Variable intensity of bioturbation.	Hemipelagic suspension settling from ice-proximal to ice-distal glacimarine/ fluvial sediment. Possible winnowing/selective deposition from currents.	Facies 3
Mc	Mudstone with clasts	Mc facies is similar to Mm facies, but contains clasts >1% in abundance. Clasts are typically granule- to pebble-sized, and the facies is commonly bioturbated, and often interbedded with Dm and Ds facies, though diatom-rich examples can be associated with DO facies.	Similar to Ms and Mm, but with ice-rafted debris.	Facies 4
DO	Diatomite	Weakly laminated to intensely bioturbated diatomite. Clasts are absent in some intervals, but dispersed and rare in others. Disarticulated shell fragments are common (millimeter- to centimeter-scale bivalves). DO facies can grade into and out of Mdo/Ms.	Pelagic ice-distal glacimarine and hemipelagic sedimentation (+/− clasts representing ice rafting processes).	Facies 5
Mdo	Diatom-rich mudstone	Similar to DO facies, but with higher mud content, and articulated bivalves are present in some intervals.	Ice-distal glacimarine sedimentation with pelagic deposition.	Facies 5
Mch	Chertified mudstone	Similar to Mdo and DO facies, but with diatom content replaced by chert.	Diagenetically altered diatomite and mudstone facies.	Facies 6
Clc	Conglomerate with lithified clasts	Matrix- to clast-supported conglomerate with subrounded to rounded clasts (granules to cobble grade) of indurated basement lithologies.	Basal debris flows fallout proximal to grounding line, submarine redeposition and winnowing by currents or channelized flow.	Facies 7
Cli	Conglomerate with intraclasts	Clast-supported conglomerate with deformed subrounded to rounded intraclasts of mudstone.	Basal debris fallout proximal to grounding line, with winnowing by currents or channelized flow.	Facies 7

Note: Detailed descriptions are presented in the equivalent facies scheme of McKay et al. (2019), but deviations from that scheme are noted here. mbsf—m below sea floor.

subglacial (sheared diamictite, Dm-sh) or ice sheet-proximal facies (massive diamictite, Dm) into grounding-line–proximal facies of conglomerate (with lithified clasts and intraclasts, Clc and Cli) or sandstone, stratified diamictite (Ds), or glacimarine mudstone with clasts (Mc), and then into progressively more distal ice shelf, glacimarine, or open-marine facies such as stratified mudstone (Ms), massive mudstone (Mm), diatom-bearing to diatom-rich mudstone (Mdo)/ chertified mudstone (Mch), and diatomite (DO) (Smith et al., 2019; Table 1).

The specific compositions and thicknesses of facies cycles and successions can vary depending on past climatic and glacial thermal regimes. Present-day Antarctic Ice Sheet mass loss is predominantly controlled by iceberg calving, by basal melting of ice shelves, and at marine grounding lines, whereas surface meltwater runoff and turbid subglacial meltwater discharge is comparatively limited today (Pritchard et al., 2012; Rignot et al., 2013; Depoorter et al., 2013; Paolo et al., 2015; Smith et al., 2020). As such, Antarctica's continental shelves are sediment starved, with glacial retreat cycles generally <1 m thick, except where they are in close proximity to highly localized subglacial meltwater channels (McKay et al., 2009; Horgan et al., 2013; Simkins et al., 2017; Prothro et al., 2018; Smith et al., 2019). This sediment starvation characterizes late Pliocene to Pleistocene interglacial sedimentation in the Ross Sea, with pelagic deposition of diatomites indicating a surface water column that lacks significant turbidity, and which is conducive to increased abundance of photosynthesizing plankton (Naish et al., 2009; McKay et al., 2009).

In glacial regimes that are warmer than present-day continental Antarctica—for example, Greenland; Norway (mainland and Svalbard); and Alaska, USA—surface meltwater exerts significant control on glacial mass balance (Vaughan et al., 2013; IPCC, 2022) by percolating through the ice to its base, which enhances dynamic ice discharge rates and results in a higher discharge of turbid meltwater via glacimarine or glacifluvial systems. As such, there are higher terrigenous sedimentation rates for sediment deposited in coastal settings during deglaciations and interglacials as compared to the Antarctic Ice Sheet margin (Powell and Domack, 1995; Cowan et al., 1999; Chu et al., 2009; Laberg et al., 2009, 2018; Dowdeswell et al., 2015; Jaeger and Koppes, 2016). Such conditions are thought to have been more common around the Antarctic margin prior to and during the Miocene (Hambrey and McKelvey, 2000; Sugden and Denton, 2004; Lewis et al., 2006; McKay et al., 2009; Passchier et al., 2011; Gulick, Shevenell, et al., 2017).

Following peak interglacial conditions, the vertical facies succession represents a progressive return to glacial proximity, and re-advance facies may either (1) continue upward toward the most grounding-line–proximal facies without evidence of erosion, or (2) be truncated by a GSE and pass abruptly into the massive diamictite of the overlying cycle, which indicates erosion by an overriding grounded ice sheet. In either case,

the top of the cycle is defined by the basal contact of the most proximal glacial facies or the GSE of the overlying cycle (Fielding et al., 2000; Powell et al., 2001; Naish et al., 2008; McKay et al., 2009).

Background: Seismic Stratigraphic Framework of the Ross Sea

A critical aspect of interpreting geological drill cores is integration with the broader stratigraphic architecture provided by seismic stratigraphy. The Scientific Committee of Antarctic Research's (SCAR) Antarctic Offshore Stratigraphy project developed a series of regional maps of eight depositional sequences in the Ross Sea (Brancolini et al., 1995). Each sequence directly relates to shifts in the climatic or tectonic-driven sedimentary regimes and is bound by unconformities titled Ross Sea unconformities (RSUs) ranging from RSU7 (Cretaceous) to RSU1 (Pleistocene; Brancolini et al., 1995; Cooper et al., 1995, 2008; De Santis et al., 1995; Luyendyk et al., 2001; Bart, 2003; Sorlien et al., 2007; McKay et al., 2022b; Pérez et al., 2022a, 2022b). The oldest and deepest sequences were formed by active rifting and extension during Cretaceous continental breakup (Luyendyk et al., 2001), and are overlain by predominantly aggradational glacimarine strata of Eocene to Oligocene age. However, progradation around bathymetric highs and stratigraphic truncations could relate to localized ice cap/sheet advances and/or local sea-level changes (Brancolini et al., 1995; Sorlien et al., 2007; McKay et al., 2022b; Pérez et al., 2022a).

Early Miocene RSU5 (ca. 18 Ma) is a widespread seismic unconformity that separates largely aggradational strata from thick overlying sequences of progradational and aggradational strata of late early to middle Miocene age (Fig. 3). Within these strata, several intra-unit discontinuities (surfaces Db, RSU4a, and Da) are inferred to represent major variations in ice sheet extent in the Ross Sea through the early to middle Miocene (De Santis et al., 1995; Marschalek et al., 2021; McKay et al., 2022b; Pérez et al., 2022a). Seismic unconformity RSU4 separates sediment between ca. 15.9 Ma and 14.2 Ma in age at Site U1521 and represents an almost shelf-wide erosional truncation that is interpreted as a marine-based ice advance (Cooper et al., 1991; Pérez et al., 2022a; Fig. 3). Above RSU4, cyclic subglacial and glacima-

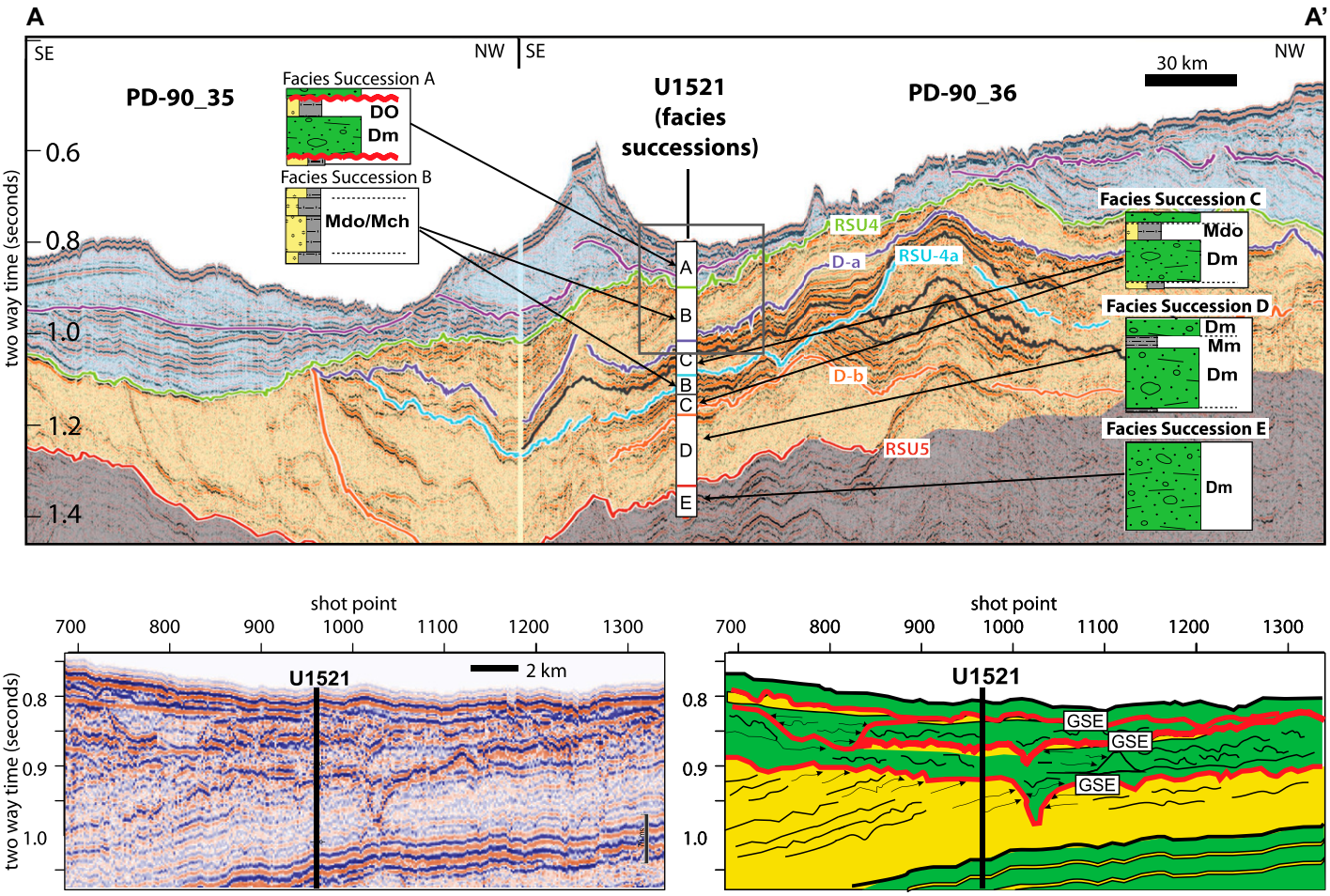

Figure 3. Top: Seismic profile from the R/V *Polar Duke* 1990 cruise (lines PD-90_35 and PD90_36; after Pérez et al., 2022a), showing the wider basin seismic stratigraphy with comparison of unconformity-bound seismic packages and the U1521 facies succession packages presented in this work (see Fig. 2). Line location is shown in Figure 1. Gray box shows the location of the uninterpreted enlarged section, and the interpreted enlarged section is shown in the lower panels. Bottom left: Uninterpreted zoomed-in section of seismic line PD-90_36. Bottom right: Interpreted zoomed-in section of seismic line PD-90_30. Green equates to diamictite-dominated sediment, and yellow indicates diatom-rich sediments. Note that lithological interpretations are schematic. DO—diatomite; Dm—massive diamictite; Mdo—diatom-rich mudstone; Mch—chertified mudstone; Mm—massive mudstone; GSE—glacial surface of erosion.

rine sedimentation is discontinuously preserved at IODP Site U1521 (De Santis et al., 1995; McKay et al., 2019; Pérez et al., 2022a), and the depocenter of progradational strata shifted toward the Eastern Basin, where a record was recovered at Site U1522 (Fig. 1; De Santis et al., 1995; McKay et al., 2019).

METHODS

Site Location

IODP Expedition 374 Site U1521 was cored in January 2018, and is located at 75°41.0351′S, 179°40.3108′W at a water depth of 573 m within the Pennell Basin of the Ross Sea (Figs. 1 and 3). Site U1521 was drilled to a depth of 650.10 m below sea floor (mbsf), with a recovery rate of 63%. Cores were collected via rotary drilling, with each core measuring 9.5 m in length. The recovered core was spilt into ~1.5 m sections. Each core was numbered sequentially, and an identifier was given for each section (e.g., core 1, section 1, has the identifier 1R-1). Recovery was lowest in the upper 100 m of the core, and improved below 100 mbsf, except for a chert and silica-cemented interval between 350 mbsf and 285 mbsf (Fig. 2). The seismic profiles PD_90_35 and PD_90_36 (Fig. 3) used to interpret the lateral and vertical distribution of the depositional facies were collected by the U.S. R/V *Polar Duke* in 1990 (Anderson and Bartek, 1992). They are single-channel reflection seismic profiles (collected with an airgun source of 2.4 L). Borehole seismic check-shot velocity was acquired during IODP Expedition 374 (using a source of 250 in^3 G guns in parallel array, and a sonic tool string with 18 geophones; McKay et al., 2019), and was used for the depth to two-way time conversion. IHS Kingdom software was used to correlate the IODP U1521 logs with seismic reflectors (Pérez et al., 2022a).

Initial Lithostratigraphic Framework

The initial shipboard lithostratigraphic descriptions developed for Site U1521 during IODP Expedition 374 included seven preliminary lithostratigraphic units that represent major shifts in sedimentary facies (McKay et al., 2019). Seven lithofacies were also defined in the shipboard proceedings, but their distribution throughout the core was not presented in detail (McKay et al., 2019). In this study, the initial lithostratigraphy for Site U1521 was refined by visual examination of sedimentary textures and structures in the cut face of the archive half of the core, and archived line-scan images (McKay et al., 2019). Bioturbation was characterized according to the methods in McKay et al. (2019) on a scale of 0 (absent) to 4 (complete). Sedimentary texture was further characterized by quantitative grain size analysis and used to refine the textural classifications assigned during the initial descriptions. Clast counts from the cut core face of grains >2 mm in size were binned in 10 cm intervals (Marschalek et al., 2021; Zurli et al., 2022). Computed tomography (CT) x-radiographs were used to supplement our descriptions, and in particular to assess the presence/alignment of gravel grains at a higher resolution than our grain size sampling or the cut core face could allow.

Our sedimentary descriptions use the classification scheme developed by the ANDRILL project (Krissek et al., 2007). Here, we present the modification of lithostratigraphic logs (based on the methods above), as well as an expanded facies scheme, to those presented in the low-resolution, preliminary descriptions of McKay et al. (2019).

Grain Size Analysis

Laser particle size analysis was conducted on 188 samples using a Malvern 3000 particle size analyzer with a Hydro large volume wet dispersion unit. Approximately 2 g of bulk sample was subsampled, with organic matter removed by hydrogen peroxide (H_2O_2; McCave et al., 1995). Diatom remains were not removed from diamictite lithofacies, as they are in lower abundance, and information on the biogenic component is relevant for identifying potential subglacial to glacimarine influences. Prior to Malvern 3000 analysis, the dry treated samples were subsampled (~0.2 g) to target an optimal obscuration value of ~15%, and dispersed in ~50 mL of 0.5 g/L sodium hexametaphosphate and agitated in a beaker placed in an ultrasonic bath for a minimum of 20 min (following the methods and recommendations of Sperazza et al., 2004, and Chewings et al., 2014). Samples were not treated with acid due to low carbonate content. Replicate samples and glass bead standards were run periodically to ensure internal consistency.

The pre-treatment process differed for 77 samples from the diatom-rich mudstone lithofacies between 203 mbsf and 85 mbsf, to include removal of biogenic matter, as shifts in terrigenous grain size in this interval may provide insights into past shifts in bottom current strength. In this interval, ~10–15 cm^3 of freeze-dried sediment were weighed (~10–20 g), and then wet sieved at 125 μm. The dry weight of the >125 μm fraction was then measured, which in these samples represents a grain size that is distinct from that of the bulk sediment population (Fig. 4). As the dominant grain size fraction in these samples is <63 μm (Fig. 4), sieving was used to avoid biases associated with outsized sand grains in samples with a fine-grained matrix (McKay et al., 2022a). However, of the 77 samples sieved, 61 samples lacked particles >125 μm, and 12 contained only trace values (<0.1%) of outsized grains >125 μm, while four samples had slightly higher (but still low) values of between 0.1% and 0.3% (Fig. 2). Although the weights of grains >125 μm in all samples are very low, and likely lack statistical significance (McKay et al., 2022a), they are from the same intervals where clast counts on the core surface are elevated.

For the size fraction <125 μm in the diatom-rich mudstone lithofacies, organic matter was removed with hydrogen peroxide (H_2O_2), and biogenic silica was removed with 1 M sodium hydroxide (NaOH) following the methods detailed in McKay et al. (2022a) and analyzed by the Malvern 3000 for grain size. Due to pervasive chert and silica cement, no grain size samples were analyzed between 324.15 mbsf and 285.30 mbsf (Fig. 2).

Natural Gamma Ray Downhole Log Data

In situ borehole logs from Site U1521 compare well to discrete physical property measurements (McKay et al., 2019). For intervals of poor core recovery, we were able to use borehole logs to develop a continuous stratigraphy (Fig. 2). Natural gamma radiation (NGR) was measured as gamma-ray, American Petroleum Industry (gAPI) units, and is a proxy for clay content (McKay et al., 2019). At Site U1521, diatomites and diatom-bearing mudstones returned lower NGR values (generally <50 gAPI) than massive diamictite and mudstone units (generally >50 gAPI). The upper 42 mbsf at Site U1521 do not contain reliable downhole log data, as the drill pipe remained in the hole above this depth during logging (Fig. 2).

Lithofacies Characterization

We conducted the first detailed study of the facies distribution throughout the core. Lithofacies are classified via a common set of lithostratigraphic characteristics, using the same lithostratigraphic and physical property methods described above (Table 1). We present a total of 11 facies, expanding on the seven facies presented in McKay et al. (2019), which are interpreted to represent specific depositional environments along a continuum from subglacial to grounding-line proximal settings, to open-marine settings with minimal glacial influence (Table 1). From this basis, we then adopt a facies succession approach, whereby an idealized facies stacking pattern based on the vertical recurrence

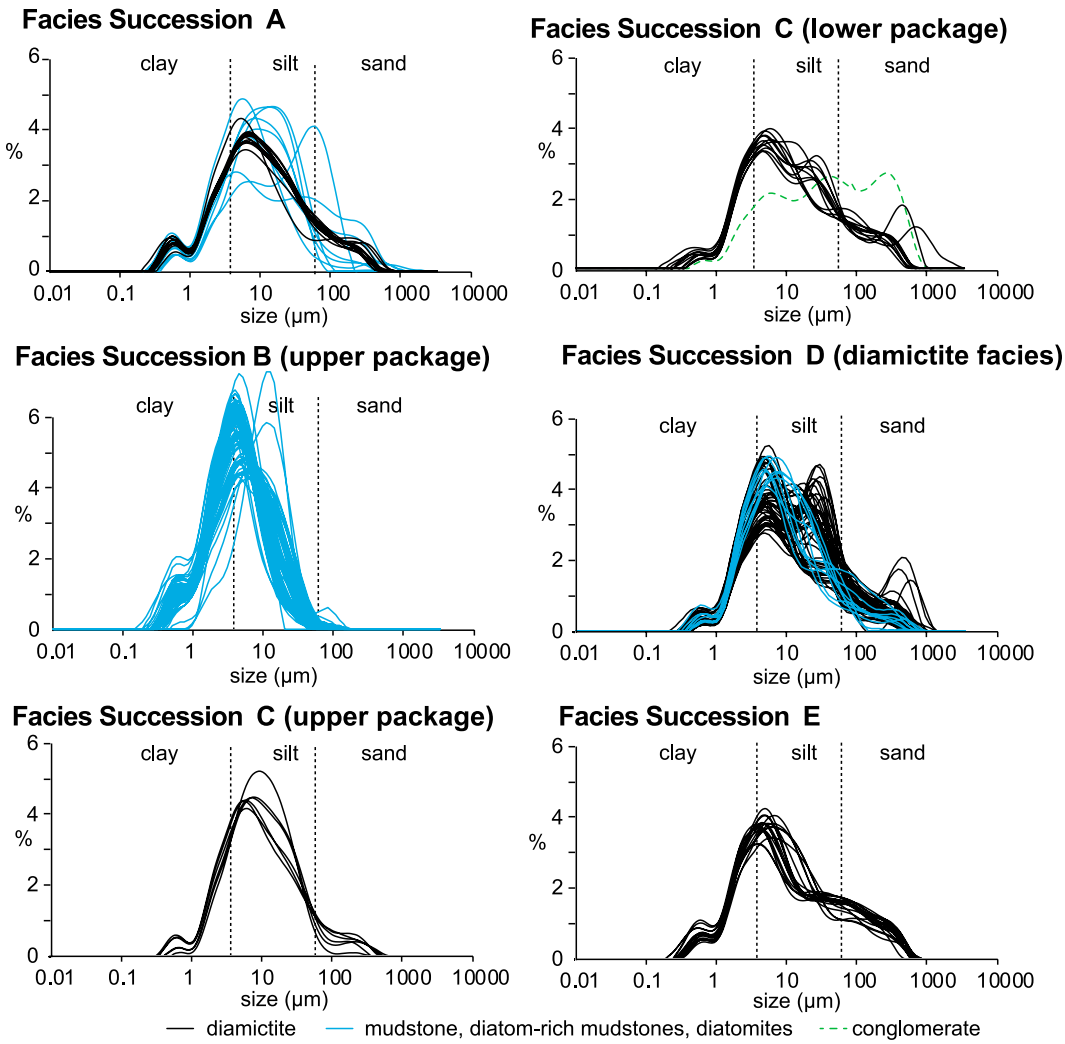

Figure 4. Grain size distributions from Facies Successions A–E, as shown in Figure 2 with groupings of similar facies.

of laterally adjacent depositional environments is used to define the cycles of glacial proximity illustrated in Figure 2. Each facies succession represents a different style of deposition during the evolution of the Ross Sea continental margin, but can be grouped into packages that may contain numerous repetitions of that facies succession (e.g., cycles). We pay particular attention to identifying deformational structures that may indicate subglacial overriding, or deformation by mass flow or loading processes that may have been associated with glacimarine sedimentation. A total of five different facies succession styles are defined. The depositional interpretations of the facies successions are then compared to the existing seismic stratigraphic framework of the Ross Sea (Pérez et al., 2022a) to provide broader regional context for our results.

Chronology

The age model constraints for Site U1521 are provided by magnetostratigraphy and biostratigraphy, $^{87}Sr/^{86}Sr$ dating of in situ macrofossils, and $^{40}Ar/^{39}Ar$ ages of reworked hornblende grains (Fig. 2; Table 2). Below 85.3 mbsf, the age model of Marschalek et al. (2021), in which a preferred and alternate solution was presented, is unchanged. The lowermost age constraint coincides with RSU5 dated at ca. 17.8 Ma at a depth of 568 mbsf (McKay et al., 2019; Marschalek et al., 2021). We largely discuss our interpretations in the context of the preferred age model of Marschalek et al. (2021), which is presented in Figure 2 (Marschalek et al., 2021)—but also discuss the caveats of considering the alternative solution for the age model. In Figure 2, we use the 2016 Geological Time Scale (GTS) to correlate our magnetostratigraphy to the published sea-level and climate curves of Miller et al. (2020), which were calibrated to the 2016 GTS. As we are not conducting orbital tuning for this paper, conversion of these paleomagnetic tiepoints to the GTS 2020 is straightforward, and the difference from the 2016 GTS is presented in Table 2.

Above 85.3 mbsf, we adopted the same methodology as Marschalek et al. (2021) to constrain the age model. First appearance datum (FAD) events are our primary age constraint, due to reworking and hiatuses, and the ranges we provide in Table 2 are based on the hybrid-age models of Crampton et al. (2016). Because of these hiatuses, the FAD of given taxa represents a maximum depositional age rather than the actual depositional age, as its true first occurrence may have been eroded. A disconformity occurs at 85.3 mbsf, and the FAD of *Denticulopsis simonsenii* (14.48 Ma) occurs in a diamictite facies immediately overlying this level. As the FAD of *D. simonsenii* is observed within the diamictite, its basal range is truncated in the Site U1521 core, which means its first appearance may be at <14.48 Ma in this interval (Table 2). There is also an absence of the *Nitzschia denticuloides* FAD (ca. 13.72 Ma) in the overlying diatom-rich mudstone between 76.4 mbsf and 75 mbsf. As this species is a ubiquitous and reliable biostratigraphic marker at other Ross Sea sites

TABLE 2. AGE MODEL CONSTRAINTS OF SITE U1521, USING THE SAME METHODOLOGY AS MARSCHALEK ET AL. (2021), BUT WITH NEW OBSERVATIONS BETWEEN 76.4 MBSF AND 0 MBSF, AND PALEOMAGNETIC CORRELATIONS TO GTS 2016 (OGG ET AL., 2016) AND GTS 2020 (OGG, 2020)

Event	Depth (mbsf)	Description	Type	Age (Ma) GTS 2016	Age (Ma) GTS 2020	Notes
A	26.6–19.41	*Cycladophora davisiana*	FAD (rad)	<ca. 2.51	<ca. 2.51	observed in core 3R-CC (0–5 cm); Florindo et al. (2013)
B	28.8–27.3	*Helotholus vema*	FAD (rad)	<ca. 4.88	<ca. 4.88	observed in core 4R-1 (68–70 cm); Florindo et al. (2013)
C	76.4–75.0	Absence *Nitzschia denticuloides*	FAD (diatom)	>13.72–14.39	>13.72–14.39	not observed in diatomites of core 9R
D	85.55–84.99	*Denticulopsis simonsenii*	FAD (diatom)	<14.14–14.48	<14.14–14.48	Marschalek et al. (2021)—max. age, Crampton et al. (2016)
E	85.72–84.99	*Denticulopsis hyalina*	FAD (diatom)	<14.73–14.76	<14.73–14.76	Marschalek et al. (2021)—max. age, Crampton et al. (2016)
F	85.55–84.99	*D. lauta*	FAD (diatom)	<14.99–15.72	<14.99–15.72	Marschalek et al. (2021)—max. age, Crampton et al. (2016)
G	85.55–84.99	*A. ingens*	FAD (diatom)	<15.52–15.83	<15.52–15.83	Marschalek et al. (2021)—max. age, Crampton et al. (2016)
H	~85.34	RSU4	Unconformity			Pérez et al. (2022a)
I	106.3–105.5	C5Br/C5Cn.1n	MPR	15.974	15.994	Marschalek et al. (2021), Ogg et al. (2016)
J	145.135–141.92	Shell fragments (average of 3)	$^{87}Sr/^{86}Sr$	16.173 ± 0.25	16.173 ± 0.25	Marschalek et al. (2021)
K	184.215–182.7	Shell fragments (average of 3)	$^{87}Sr/^{86}Sr$	16.172 ± 0.25	16.172 ± 0.25	Marschalek et al. (2021)
L	196.785	Shell fragments	$^{87}Sr/^{86}Sr$	16.26 ± 0.24	16.26 ± 0.24	Marschalek et al. (2021)
M	209–205	C5Cn.1n/C5Cn.1r	MPR	16.268	16.261	Marschalek et al. (2021), Ogg et al. (2016)
N	222.43–222.03	Hornblende grain (150–300 μm)	$^{40}Ar/^{39}Ar$ date	16.74 ± 0.90	16.74 ± 0.90	Marschalek et al. (2021)
O	272.03–269.83	Hornblende grain (150–300 μm)	$^{40}Ar/^{39}Ar$ date	17.08 ± 1.20	17.08 ± 1.20	Marschalek et al. (2021)
P	272.65	Shell fragments	$^{87}Sr/^{86}Sr$	16.30 ± 0.23	16.30 ± 0.23	Marschalek et al. (2021)
Q	286.1	*N. grossepunctata*	FAD (diatom)	15.87–15.94	15.87–15.94	Marschalek et al. (2021), Crampton et al. (2016)
R	286.1	*F. maleinterpretaria*	LAD (diatom)	16.41–16.5	16.41–16.5	Marschalek et al. (2021), Crampton et al. (2016)
S	286.1	*S. cheethamii*	FAD (diatom)	16.94	16.94	Marschalek et al. (2021), Crampton et al. (2016)
T	286.1	*D. maccollumii*	FAD (diatom)	16.77–17.05	16.77–17.05	Marschalek et al. (2021), Crampton et al. (2016)
U	286.1	*N.17 Schrader*	FAD (diatom)	16.94–17.16	16.94–17.16	Marschalek et al. (2021), Crampton et al. (2016)
V	286.2	RSU4a	Unconformity	16.3–17	16.3–17	Pérez et al. (2022a)
W	344.6–337.4	C5Cr/C5Dn	MPR	17.235	17.154	Marschalek et al. (2021), Ogg et al. (2016)
X	373.38	Hornblende grain (>150 μm)	$^{40}Ar/^{39}Ar$ date	19.17 ± 0.35	19.17 ± 0.35	Marschalek et al. (2021)
Y	380	Db	Unconformity	17.25–17.45	17.25–17.45	Pérez et al. (2022a)
Z	400.5–397.25	C5Dn/C5Dr.1r	MPR	17.533	17.466	Marschalek et al. (2021), Ogg et al. (2016)
AA	450.57–450.52	*Thalassiosira* sp. cf. *T. bukryi*	Occurrence	17.7–17.4	17.7–17.4	Marschalek et al. (2021), Crampton et al. (2016)
BB	517.2–515.1	C5Dr.1r/C5Dr.1n	MPR	17.717	17.634	Marschalek et al. (2021)
CC	526.8–524	C5Dr.1n/C5Dr.2r	MPR	17.740	17.676	Marschalek et al. (2021)
DD	567.95	RSU5	Unconformity	17.8–18.6	17.8–18.6	Pérez et al. (2022a)

Note: mbsf—m below sea floor; FAD—first appearance datum; LAD—last appearance datum; MPR—magnetic polarity reversal; RSU—Ross Sea unconformity.

(Cody et al., 2008; Levy et al., 2016), these constraints place the interval between 85.3 mbsf and 75 mbsf as being deposited between <14.48 Ma and >13.72 Ma. We infer a hiatus at 85.3 mbsf of at least ~1.7 m.y., which separates strata between ca. 15.95 Ma and 14.2–13.6 Ma in age (Fig. 2). The FAD of the radiolarian *Helotholus vema* at 27.3 mbsf, and *Cycladophora davisiana* at 19.41 mbsf, suggest that these depths are younger than 4.88 Ma and 2.51 Ma, respectively (Table 2; Florindo et al., 2013).

RESULTS AND DISCUSSION

Lithofacies Successions

Using the previously established criteria described in the Background and Methods sections to define glacial proximity, and the lithofacies described in Table 1, we have identified at least 16 depositional cycles representing shifts in grounding-line proximity at Site U1521 (Fig. 2). However, the characteristics of each cycle vary throughout the core, and below we define five types of depositional facies successions containing one or more vertically stacked cycles. In Figure 2, we show the down-core occurrence of Facies successions E through A, which are each grouped into seven distinct stratigraphic packages within the core. Depositional-specific interpretations are provided after each Facies Succession description.

Facies Succession E—Massive Diamictite

Description. Facies Succession E is an extended interval of a single facies occurrence, which is defined by massive diamictite facies (Dm) with rare millimeter- to centimeter-scale mudstone (Ms) beds. In Site U1521, these facies occur in a single package at the base of the site from 650.10 mbsf to 567.95 mbsf. There are textural variances within the massive diamictite facies that occur as decimeter-scale variations of mud and sand in the matrix, as well as clast content increases and decreases (Fig. 2). Diamictites throughout Facies Succession E display a relatively consistent distribution, but sand content is elevated compared to diamictites in other parts of the core, and there is also a more prominently defined fine silt mode (Fig. 4).

Facies Succession E contains shell fragments, carbonate concretions, and networks of veins throughout. The mottled matrix texture in some intervals is interpreted as bioturbation, and vein networks are more abundant. The age constraints linked to Facies Succession E indicate an age of >17.8 Ma, and the succession lies below RSU5 (Pérez et al., 2022a; Marschalek et al., 2021). The Facies Succession E package displays reversed magnetic polarity, but a confident correlation to the geomagnetic time scale is not possible (Marschalek et al., 2021).

Depositional setting. Facies Succession E is interpreted to represent an extended period of massive diamictite (Dm) deposition in a glacimarine setting. The lack of variation in facies suggests that although marine-terminating glaciers were present throughout the deposition of this package, a major shift in grounding-line proximity to the site did not occur during this period. Although the homogeneous nature of this interval means we cannot rule out subglacial deposition, possible bioturbation weights our interpretation toward glacimarine deposition. The grain size distributions are also notably different from those of other diamictites in the cores, with consistently higher sand content, and a well-sorted silt mode (Fig. 4). This is tentatively interpreted as reflecting deposition of glacimarine sediment, with the presence of low-energy currents acting to sort the fine fraction.

Facies Succession D—Massive to Stratified Diamictite with Mudstone Laminae and Beds

Description. Facies Succession D consists of massive to stratified diamictite (Dm/Ds) overlain by massive to stratified mudstones (Mm/Ms) that form cycles tens of meters thick (Figs. 2 and 5). The diamictites range from clast-rich to clast-poor and have a variable sand content (10%–20%); occasionally, sand content drops below 10% and the facies is classified as a mudstone (Mm or Mc). The base of the Dm facies consists of sharp to gradational contacts with minor deformation, and there is a lack of the extensive deformational and shearing features that define GSEs as described in the background section. The diamictites include common disarticulated shell fragments and occasional diatoms, although most of the original diatom content is likely diagenetically altered (McKay et al., 2019). Vein networks occur in matrix material, and the surface of the core has an appearance that is consistent with bioturbation—although in these coarse-grained lithologies, confirmation of bioturbation is difficult (Fig. 6). Mudstones in Facies Succession D range in thickness from sub-centimeter laminae commonly interstratified with facies Ds (Fig. 5) to meter-scale beds of massive or bioturbated mudstone. Thin beds and laminae of mudstone (Mm, Ms, and Mc) display sharp upper and lower contact surfaces with the diamictite facies, and often form continuous, inclined wavy laminae (Fig. 6). Thicker beds of facies Mm and Mc have gradational contacts, and appear to have characteristics similar to those of the diamictites, but have a sand content that drops below the 10% cutoff for definition as a diamictite (Krissek et al., 2007; Fig. 2). The diamictite beds also display consistent, inclined alignments of clasts above and below these mudstone beds, which are commonly at the same angle as the mudstone beds (Fig. 6). Mudstone beds also contain disarticulated shell fragments, occasional carbonate concretions, and in some instances they display silica cementing—particularly in intervals showing pervasive bioturbation.

Four cycles of Facies Succession D occur between 567.95 mbsf and 379.82 mbsf (188.13 m), which covers a 400 k.y. interval between ca. 17.8 Ma and 17.4 Ma (mainly within Chron C5Dr; Marschalek et al., 2021). An ~22-m-thick mudstone bed with clasts (Facies Mc) is observed between 467.7 mbsf and 445.7 mbsf, while an 11-m-thick mudstone bed with lower clast content (Facies Mm) is observed between 527 mbsf and 516 mbsf. The beds consist of slight to highly bioturbated mud, with the lower bed being more heavily bioturbated, particularly at its basal contact (Fig. 5). The upper-bounding surface of the package of Facies Succession D cycles at 379.82 mbsf is associated with seismic surface D-b (Pérez et al., 2022a; Marschalek et al., 2021; Figs. 2 and 3).

Diamictites within Facies Succession D have a highly heterogeneous distribution, with variable sand percentages and muddy diamictites that contain coarse to fine silt modes. Facies classified as mudstone have a distribution similar to that of the muddy diamictite facies in this succession, but lack a coarse silt mode and have reduced sand (<10%) and clast contents (Figs. 2 and 4).

Depositional setting. Facies Succession D is interpreted to represent repeated cycles of grounding-line–proximal glacimarine diamictite infilling a continental shelf basin. The age model and facies interpretations indicate that the diamictite facies were emplaced rapidly, while previous provenance studies of this interval imply an expanded West Antarctic Ice Sheet proximal to Site U1521 (Marschalek et al., 2021). The thickness of this package of Facies Succession D indicates that at least 188 m of accommodation was available at this site, which implies that a water column of at least this thickness was present during the onset of deposition. The progradational pattern of the deposit is also supportive of deposition in a proglacial setting (Pérez et al., 2022a), with rapid sediment supply outpacing the subsidence rate (Fig. 3). The sharp, wavy lower contacts with the mudstone laminae and interbeds display no evidence of deformation associated with glacial overriding. Indeed, the mudstone facies commonly occur as thin mudstone drapes or wavy laminae (Figs. 5 and 6), which likely represent periods of reduced glacimarine supply. The characteristics of the mudstone laminae are consistent with similar fine-grained wispy laminae deposited in low-energy, deep-water settings that result in suspension settling of only the finest grained muds (Rebesco et al., 2014). The presence of thin mudstone laminae, and bioturbated mudstone interbedded with thick massive diamictites, are broadly consistent with the late Pleistocene depositional facies models directly in front of trough mouth fan deposits offshore of Greenland (Ó Cofaigh et al., 2013), where the massive diamictites comprise glacigenic debris flows. Thicker intervals of massive/bioturbated mudstone (Mc and Mm) occur in two cycles of Facies Succession D at 445.8 mbsf (~22 m thick) and 515.7 mbsf (11.2 m thick), and appear to be the result of gradational reductions in coarse silt and sand content. The bioturbation and thickness of these two beds suggest that although glacimarine and debris flow sediment supply persists through this interval, it is in a lower energy/more distal setting (cf. McKay et al., 2009) than other cycles in this package. The highly heterogeneous grain size distribution throughout this package, with well-defined but variable coarse to fine silt modes, is suggestive of periodic shifts in glacimarine sediment supply and meltwater input relating to proximity to a grounding line, with suspension settling or winnowing regulated by marine currents (Figs. 2 and 4).

Facies Succession C—Diamictite Overlain by Mudstone and Diatom-Bearing Mudstone

Description. The base of Facies Succession C is characterized by massive diamictite (Dm) that is typically overlain by stratified diamictite (Ds) or thin beds of stratified and massive mudstone (Ms and Mm) and diatom-rich mudstone (Mdo) that are decimeter-scale in thickness (Fig. 7). The basal Dm facies have variable lower contact characteristics (e.g., sharp to gradational), and lack the extensive deformational features that are consistent with shearing. However, minor ductile deformation or loading features may be present both at the contact and within the diamictite itself. These features do not demonstrate the same characteristics as the extensive and more definitive shearing structures that are concentrated at the basal contact of the Facies Succession A cycles. Structures indicative of rotation or shearing are usually a single occurrence isolated from other deformational features (Fig. 7). Similar styles of deformation are also observed in other facies of this succession, and not just associated with the basal contact of the Dm facies. The diatom-rich mudstone (Mdo) and stratified mudstone facies may also include rare wavy laminae, augen-like lens features around large clasts that appear to have been rotated, low-angle or normal faulting, and flame structures (Fig. 7). In addition, shell fragments are common in the diamictite (Fig. 7; McKay et al., 2019), which has a distinctive mottled pattern that we attribute to bioturbation (Figs. 7 and 8C).

Several cycles of Facies Succession C show subtle differences from this idealized pattern, with intervals of stratified mudstone (Ms) that transition into interlayered diamictite and mudstone up-section. In two cases, the base of a cycle overlies conglomerate facies, one at ~276.45 mbsf with deformed mudstone intraclasts (Cli), and one at 379.4 mbsf with clasts of basement lithologies (Clc; Figs. 8A and 8B).

Facies Succession C cycles also occur within two discrete packages in Site U1521, with an upper package between 282.22 mbsf and 209.17 mbsf, and a lower package between 379.82 mbsf and 324.15 mbsf (Fig. 2). The basal cycles of both of these packages overlie the conglomerate beds described above. We identified four cycles in the upper package of Facies Succession C, but the number of cycles in the lower package is harder to define due to lower recovery. Thus, we conservatively assign two cycles, but downhole

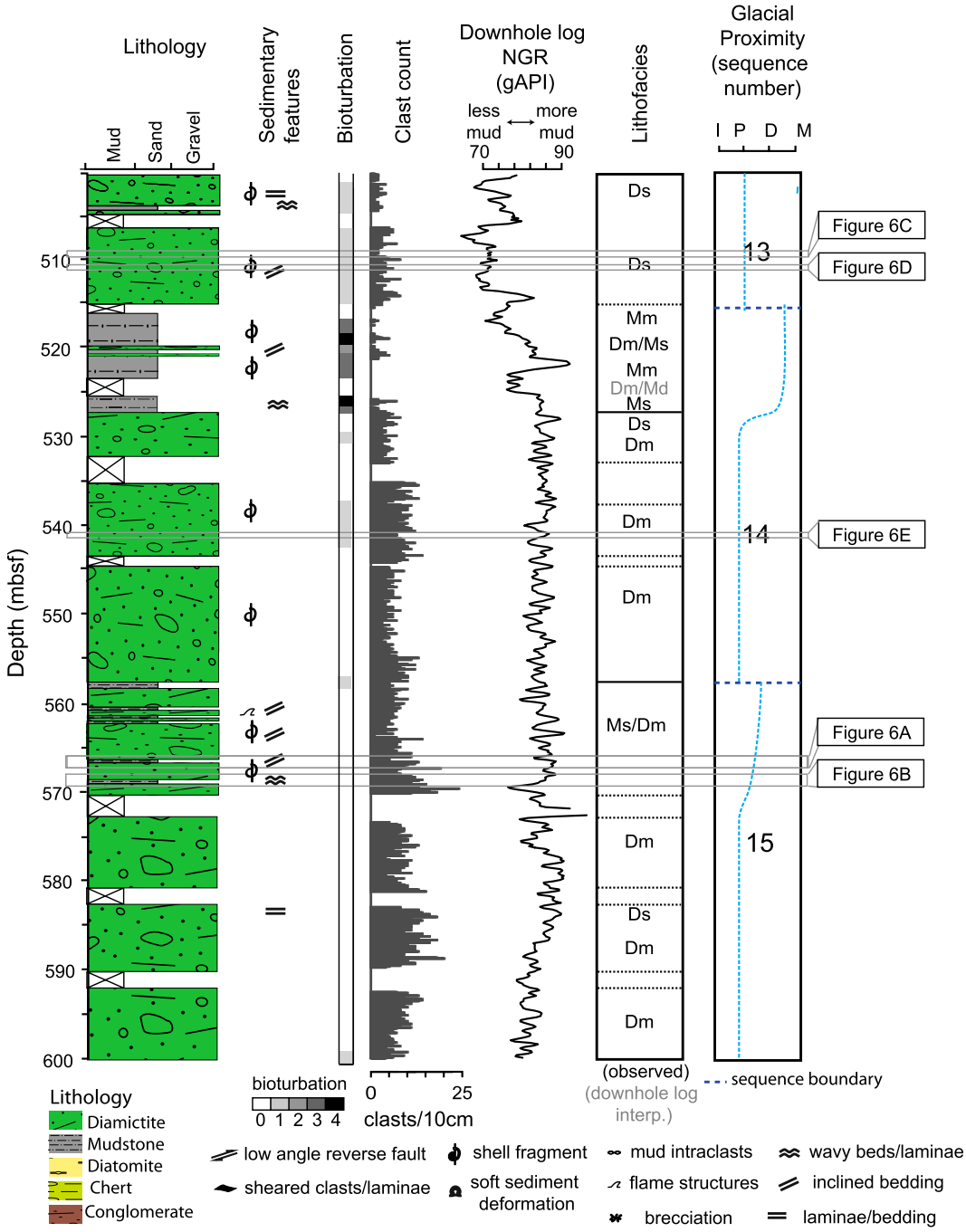

Figure 5. Stratigraphy of Facies Succession D cycles in the 600–500 m below sea floor (mbsf) interval of Site U1521. From left to right: Lithology (showing intervals of missing recovery), sedimentary features (see Fig. 5 for symbol legend), bioturbation intensity; and clast abundance; continuous downhole log natural gamma radiation (NGR, which is wireline log-matched depth below seafloor and likely offset from cores presented on the mbsf depth scale, as recovered core could be placed anywhere in the 9.5 m core run); lithofacies and cycle numbers with glacial proximity curve (blue line; I—ice contact, P—ice proximal, D—ice distal, M—open marine), with non-glacially eroded sequence boundaries (SB; dark blue dotted line). Locations of core photos in Figure 6 are also indicated. Dm—massive diamictite; Ds—stratified diamictite; Mm—massive mudstone; Ms.—stratified mudstone.

NGR suggests that additional cycles could exist (Fig. 2). The lower package of Facies Succession C displays lithologies and downhole log properties that are consistent with the upper package (Fig. 2), except that the lower package is below the opal cristobalite–tridymite (opal-CT) boundary and the diatom-rich mudstone (Mdo) is replaced by chertified and silica-cemented mudstones (Mch).

Diamictites in the upper package of Facies Succession C have a grain size distribution that is indicative of a muddy diamictite, with reduced sand content compared to Facies Succession E diamictites, but the diamictites are slightly less homogeneous than those in Facies Succession A and contain more coarse silt and less sand (Fig. 4). Diamictites in the lower package of Facies Succession C are more poorly sorted, with an even more heterogeneous distribution and elevated sand fraction compared to the upper package.

The upper package of Facies Succession C was deposited between 16.30 Ma and 16.27 Ma, within Chron C5Cn.1r (Marschalek et al., 2021). The age of the lower package is less well constrained and is either in Chron C5Dn (ca. 17.53–17.24 Ma) or subchron C5C.3n (16.72–16.54 Ma).

Depositional setting. Facies Succession C is interpreted as representing cyclic deposition of proximal glacimarine to possible subglacial facies (Dm), which are overlain by facies consistent with glacimarine settings that are progressively distal to the ice sheet grounding line (Ds, Ms, Mm, Mdo, and Mch). The seismic interval corresponding to Facies Succession C contains high-amplitude and laterally continuous reflectors that are consistent

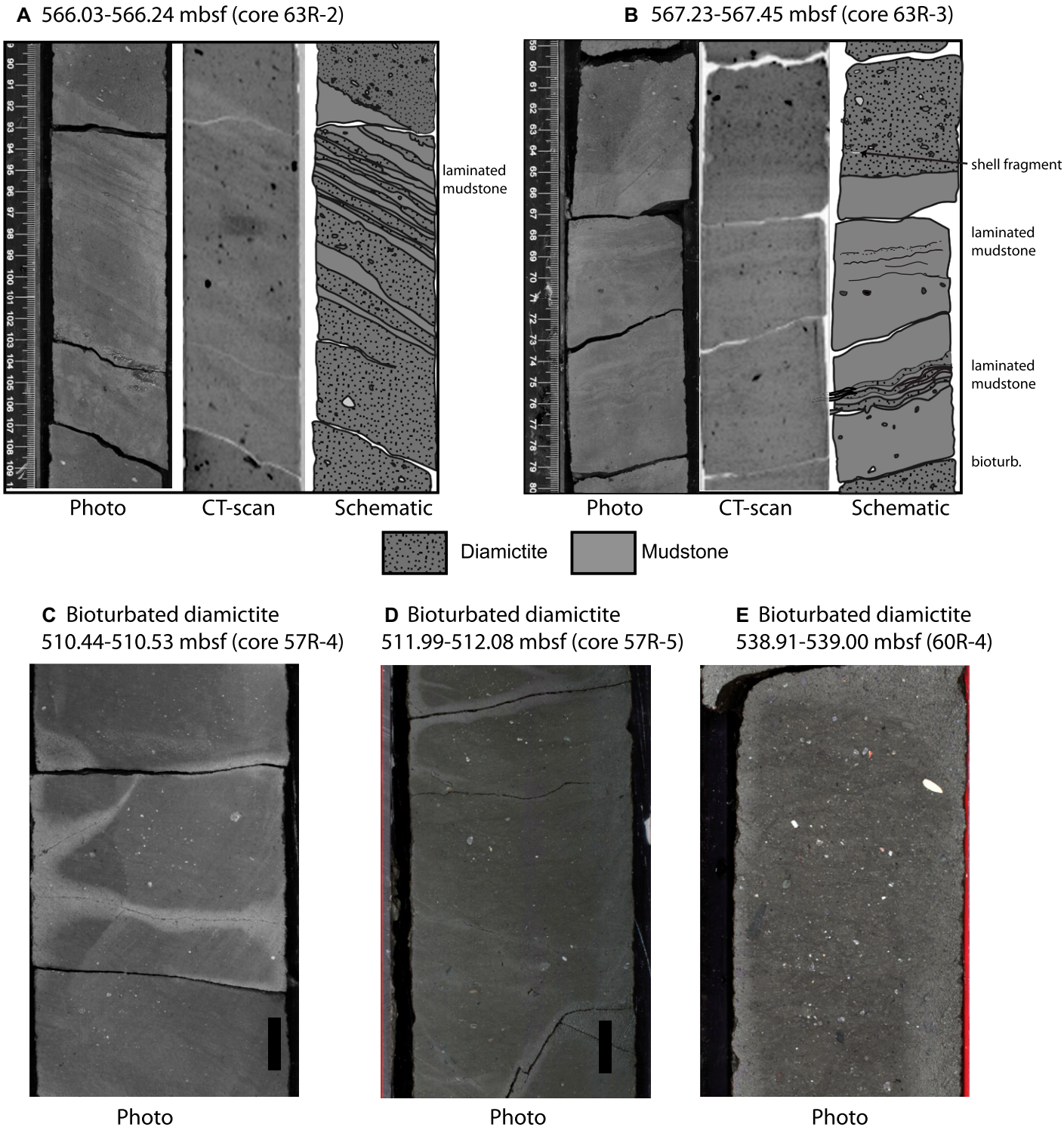

Figure 6. (A, B) Core photographs, CT-scan images, and interpreted examples of interbedded diamictite and mudstones facies in Facies Succession D cycles (A is core 63R-2; B is 63R-3). (C–E) Examples of possible bioturbation (bioturb.) in diamictite facies of Facies Succession D cycles (photos are contrast-enhanced to highlight features). (C is core 57R-4; D is core 57R-5; E is core 60R-4.)

with the alternation of low- and high-density sediments (Fig. 3). Although glacial overriding cannot be ruled out, the deformational features are more subtle than in typical GSEs (cf. Facies Succession A), and are also consistent with rapid sediment infilling and loading-based deformation. The intraclast conglomerate (Cli) is similar to the granulated/pelletized facies observed in post–Last Glacial Maximum (LGM) grounding-line retreat sequences that are interpreted to represent the melt-out of basal debris from floating ice in the vicinity of a grounded ice stream—the environ-

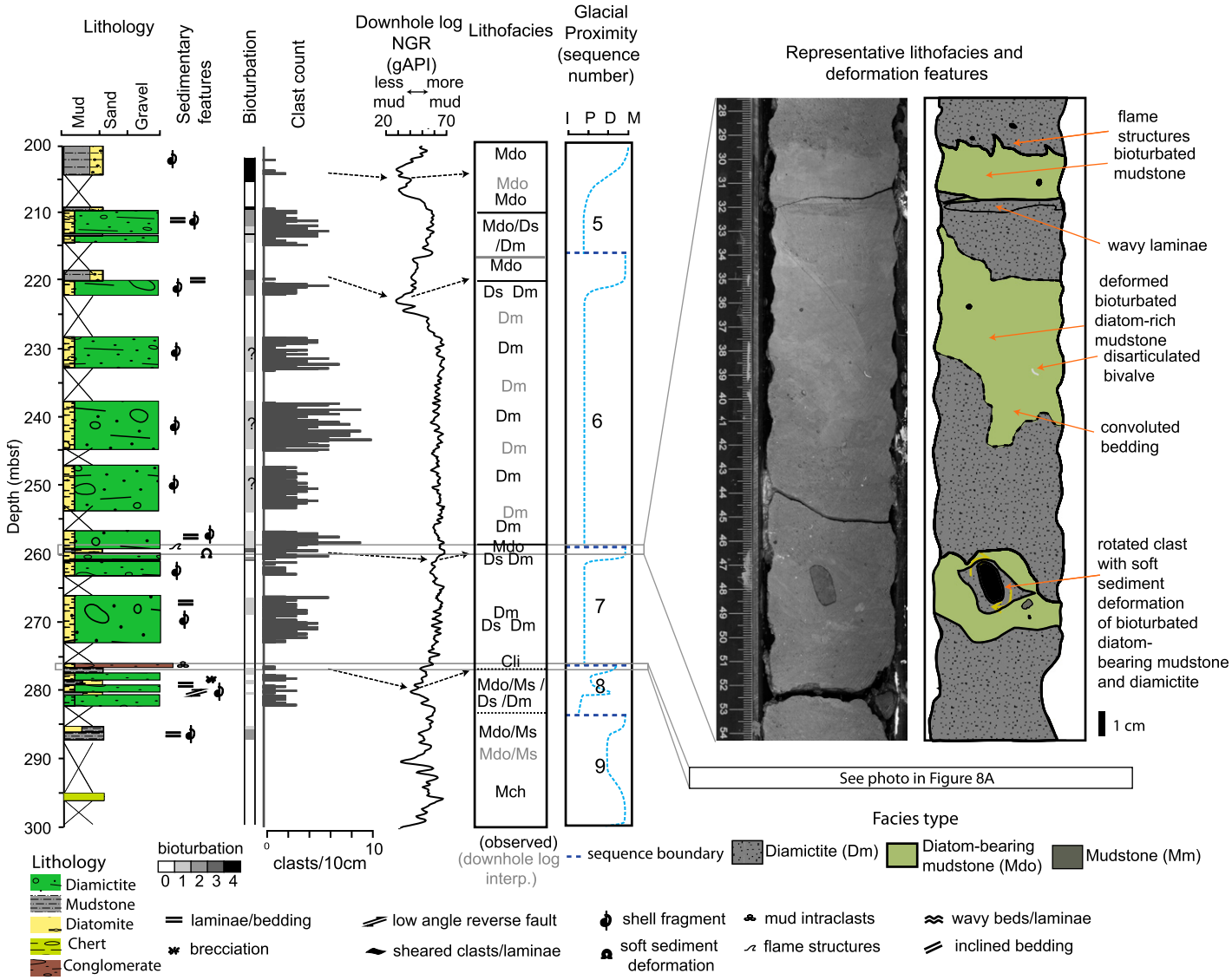

Figure 7. Stratigraphy of Facies Succession C cycles in the 300–200 m below sea floor (mbsf) interval of Site U1521. From left to right: Lithology (showing intervals of missing recovery); sedimentary features (see Fig. 5 for symbol legend); bioturbation intensity; clast abundance; downhole log Natural Gamma Radiation (NGR, which is wireline log-matched depth below seafloor and likely offset from cores presented on the mbsf depth scale, as recovered core could be placed anywhere in the 9.5 m core run); lithofacies; cycle numbers with glacial proximity curve (blue line; I—ice contact, P—ice proximal, D—ice distal, M—open marine), with non-glacially eroded sequence boundaries (dark blue dotted line); photograph (contrast enhanced) of deformational features in diamictite facies at ~260 mbsf (core 28R-3) and locations of core photo shown in Figure 8.

ment in which these pellets form (Domack et al., 1999; Cowan et al., 2012; Smith et al., 2019). The deformed nature of the intraclasts is suggestive of loading by overlying sediment, as deformation is defined by horizontal elongations, and the intraclasts have a wavy appearance but are not highly sheared (Fig. 8).

The conglomerate beneath the lower package is dominated by basement lithologies that include basalt, metasediments, and granite (Marschalek et al., 2021; Zurli et al., 2022). Similar facies are interpreted as representing channel systems in a proglacial setting (Powell and Molnia, 1989; Powell and Domack, 1995; Dowdeswell et al., 1998; Hambrey and McKelvey, 2000; McKay et al., 2009). Consequently, these conglomerates underlying the lowermost cycles in these Facies Succession C packages are interpreted as having been deposited proximal to a channel system near an ice sheet grounding line, while the overlying diamictites at the base of Facies Succession C packages represent either the overriding of ice or rapid sedimentation by mass flow in a glacimarine setting that was proximal to the grounding line during glacial maxima.

The more heterogeneous nature and slightly coarse silt mode of the diamictite grain size frequencies are consistent with those of Last Glacial Maximum glacimarine deposits located proximal to an ice sheet grounding line on the foreset of a grounding zone wedge (Prothro et al., 2018). However, some samples, such as the conglomerate and some of the diamictites in the lower package, could have been influenced by winnowing or meltwater discharge (Fig. 4).

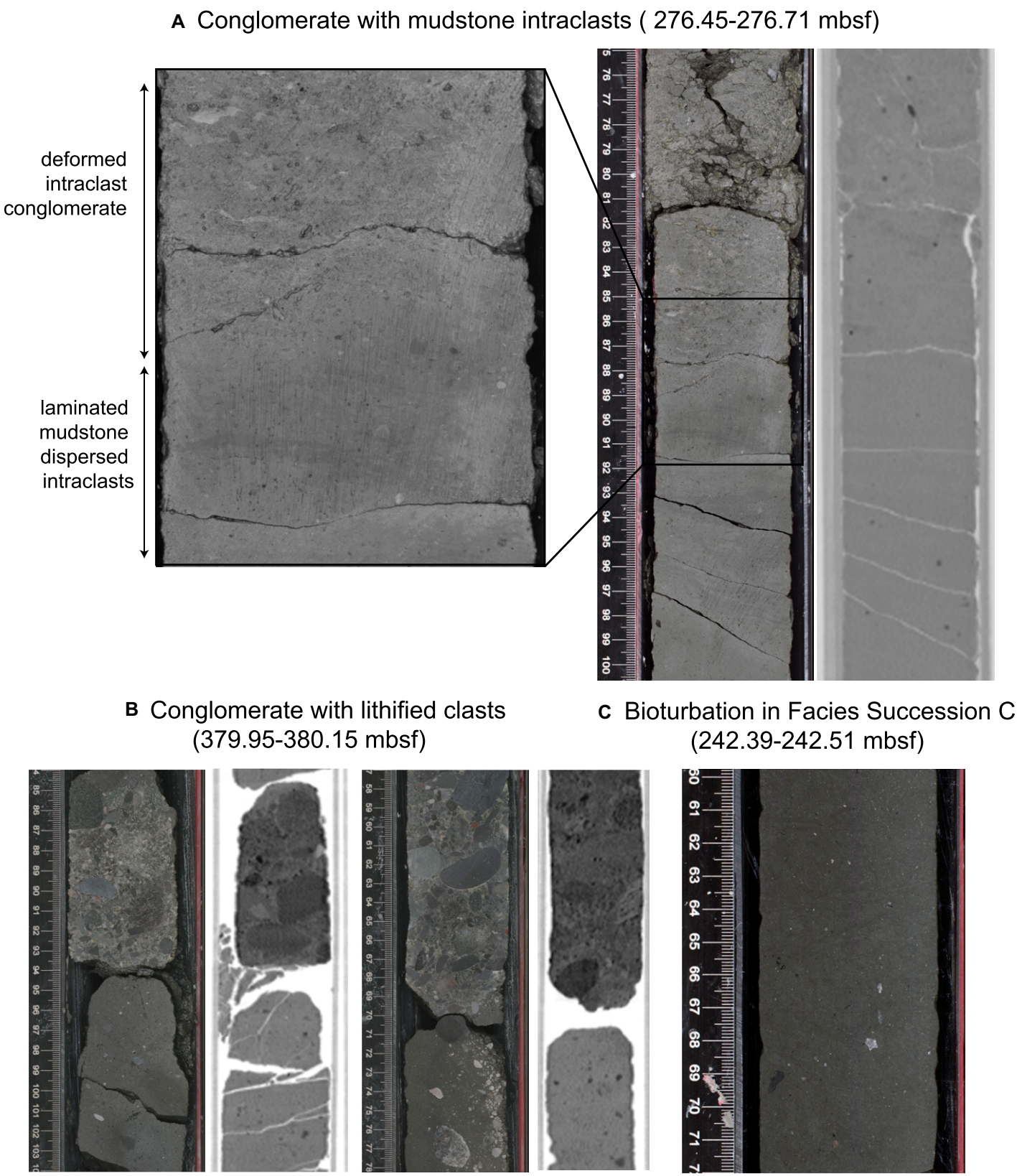

Figure 8. Core photographs and computed tomography scan images of (A) conglomerate with intraclast facies and its basal contact (core 30R-1; photo is contrast-enhanced); (B) conglomerate with lithified clast facies (core 43R-4); (C) a bioturbated diamictite (core 26R-4; photo is contrast-enhanced). All examples are from Facies Succession C cycles. mbsf—m below sea floor.

In the cycles of Facies Succession C located higher in both of these packages, there is an absence of grounding-line–proximal facies, such as stratified coarse sandstones and conglomerates (Facies Cli and Clc), which suggests that the grounding line was more distal than is interpreted for the cycles at the base of each of these packages.

Facies Succession B—Stratified Diatom-Rich Mudstone/Chertified Mudstone

Description. Facies Succession B is characterized by interbedded mudstones (Facies Mm/Ms) and diatom-rich mudstones or chertified mudstones (Mdo/Mch). Cyclic sequences that define this association occur in two packages within the Site U1521 stratigraphy—an upper package between 209.18 mbsf and 85.34 mbsf and a lower package between 324.15 mbsf and 285.30 mbsf. Both facies are bioturbated and contain interbeds ranging from 1 m to >16 m thick. Contacts between beds are gradational, which makes the identification of cycle boundaries (e.g., laterally conformable equivalents of GSEs) difficult. Consequently, we characterize these successions as sub-cycles in Figure 2. Clast counts indicate sparse peaks of coarse gravel, while sieve analysis indicates a general lack of grains >125 μm, except for a short interval of slightly elevated clast/sand content below 180 mbsf (Fig. 2). Downhole NGR displays the lowest values in the core (10–30 counts/s), which are reflective of the high biogenic silica content, although decimeter-scale variations highlight variable terrigenous mud content (Figs. 2 and 9) that is consistent with the visual observations of cyclic shifts in Facies Mm/Ms and Mdo/Mch. However, there are persistently higher mud concentrations in the lowermost sub-cycles of the upper package of Facies Succession B (209.18–161 mbsf), which also contain more coarse sand and gravel-rich beds. The terrigenous component of the diatom-rich mudstones throughout Facies Succession B displays well-sorted distributions with very fine to fine silt modes, and almost all of the samples lack sand (Fig. 4).

In the lower package of Facies Succession B, diatoms are absent below 285.3 mbsf, and mudstones are either silica-cemented or chertified. The presence of cherts caused low and sporadic recovery. Consequently, interpretations of the continuous stratigraphic succession in this interval are derived from downhole log data. These data show trends and cycles similar to those of the upper package of Facies Succession B (Fig. 9), with NGR values consistently higher below ~307 mbsf but highly cyclic at the meter scale. Between ~332 mbsf and 307 mbsf, the average amplitude of NGR variability is ~10 counts/s, but with an up-section trend to lower values (total range: 70–50 counts/s). However, between 307 mbsf and 287 mbsf, the amplitude increases to ~20 counts/s, with values as low as 30 counts/s (Figs. 2 and 9). As with the upper package of Facies Succession B, this implies an up-section decrease in terrigenous mud content through this interval and an increase in diatom content, but with cyclic variations at the meter to decimeter scale.

The depositional age of the upper package of Facies Succession B sub-cycles in the 209.17–85.34 mbsf interval is tightly constrained between ca. 16.3 Ma and ca. 15.95 Ma, with the contact between overlying cycles above 85.34 mbsf representing a hiatus of at least 1.7 m.y. (Marschalek et al., 2021; Table 2). The age of the lower package of Facies Succession B (324.15–285.30 mbsf) is less certain due to a lack of diatom-based age constraints, but existing constraints indicate it is either 16.54–16.47 Ma (in Chron C5Cn.1r) or ca. 17.0–16.7 Ma (Marschalek et al., 2021; Fig. 2).

Depositional setting. Both packages of Facies Succession B are interpreted as reflecting biogenic deposition in open water with a terrigenous influence from glacimarine–glacifluvial meltwater in a subpolar glacial regime and/or hemipelagic processes (Ó Cofaigh et al., 2001; Dowdeswell et al., 2002; McKay et al., 2009). Coarse sand and gravel clasts are present in the lowermost 15 m of the upper package of Facies Succession B (209.17–194 mbsf), which implies the presence of some marine-terminating ice in the Ross Sea at that time. However, there is a general lack of grains exceeding 125 μm above ~180 mbsf, which implies an absence of significant ice-rafting from large marine-terminating glaciers in the Ross Sea between ca. 16.2 Ma and 15.95 Ma. Facies Succession B is interpreted as the most ice distal facies in the study.

The lower package of Facies Succession B is harder to interpret at the same resolution, due to postdepositional diagenesis leading to poor core recovery. As with the upper package, decreasing mud content higher in the package (Figs. 2 and 9) indicates that the site was becoming increasingly distal from the grounding line as the ice sheet retreated toward a terrestrially terminating margin. Differences in the absolute values of downhole log NGR are likely due to compaction and postdepositional diagenetic transition through the opal-CT boundary in the lower package, whereby diatom-rich mudstone (Mdo) facies are a facies correlative to chertified mudstone (Mch). The sub-cycles of variable mud abundance (Figs. 2 and 9) may represent either small-scale readvance of the grounding line during a cooling event, enhanced meltwater runoff in a warmer climate, or productivity changes (Ó Cofaigh et al., 2001; Dowdeswell et al., 2002; McKay et al., 2009). Future comparison of these terrigenous inputs with paleotemperature and paleoproductivity proxies is required to resolve which of these processes exerts the dominant control on these sub-cycles.

The well-sorted distributions with a variable silt-sized mode suggest that bottom current speeds were variable but relatively low, and below storm wave base (Dunbar and Barrett, 2005). Almost all of the samples lack sand and gravel clasts, which suggests that glacimarine input was minimal in this interval (Figs. 2 and 4).

Facies Succession A—Diamictites with a Basal GSE Overlain by Diatomite or Diatom-Rich Mudstone

Description. The base of this succession is defined by a sharp lower contact containing multiple lines of evidence of shearing (Dm-sh), which passes up into a massive diamictite (Dm) (Figs. 10 and 11). The Dm facies then transition sharply into beds of diatom-bearing mudstone (Mdo), or in some cycles mud-rich or mud-poor diatomite (DO) that are highly variable in thickness, ranging from a few centimeters up to 6 m. Cycles of Facies Succession A are restricted to

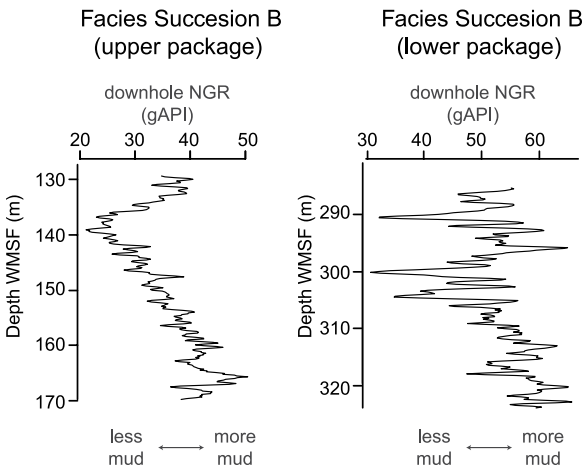

Figure 9. Natural gamma radiation (NGR) downhole log measured in American Petroleum Institute units (gAPI) in Facies Succession B cycles. Depth scale is wireline log-matched depth below seafloor (WMSF).

the uppermost 85 m of the core, which spans the middle Miocene to present (ca. 14.2–0 Ma). Although recovery is poor, at least three depositional cycles with clearly defined deformational surfaces at their bases were recovered, and a similar number of glacially formed erosion surfaces are noted in seismic profiles across the site (Fig. 3).

Differences in lithification and diatom content in each of these cycles suggest the likely presence of large time gaps between deposition of these cycles. The uppermost cycle occurs above 19.03 mbsf and is consistent with post-LGM (20 ka) retreat sequences observed in nearby piston cores (Salvi et al., 2006; Prothro et al., 2020). However, a potential GSE at ~7.7 mbsf within this cycle is noted, based on ductile and brittle deformational features within a diamictite-rich interval (Fig. 11A). However, poor recovery, a lack of downhole logging, and limited resolution in the seismic profile (Fig. 3) precludes the identification of sequence boundaries in this interval. Diamictites throughout Facies Succession A display a highly homogeneous grain size distribution that is indicative of a muddy diamictite, but with a fine silt mode. Mudstone and diatomite facies are generally better sorted but have variable modes that range from fine silt to coarse silt (Fig. 4).

Cycle 2 occurs between 74.98 mbsf and 19.03 mbsf (Fig. 10), with a basal sheared diamictite (Dm-sh) facies overlying an interpreted GSE (Fig. 11B), which grades into a carbonate-cemented muddy diamictite (Dm) with moderate bioturbation, and then into a mud-rich diatomite (DO). Downhole log values of NGR show low values (average: ~35 gAPI) in a zone of non-recovery between 60 mbsf and 38.2 mbsf that are consistent with values of diatom-rich mudstones observed deeper in the site. This interval is bracketed by diamictite facies (Dm and Ds), which suggests the possibility of a fourth cycle that was not recovered. However, there is no evidence of an additional glacial erosion surface in seismic profiles associated with an extra cycle (Fig. 3), which suggests this downhole log NGR signal may be the result of edge effects related to the presence of the drill pipe in the upper part of the hole (Fig. 10). The maximum age of the diatomite (37.7–19.03 mbsf) in Cycle 2 is constrained by the FAD of the radiolarian *Helotholus vema* (ca. 4.88 Ma), and indicates that it is Pliocene or younger in age (Table 2).

Cycle 3 (85.34–74.98 mbsf) also contains a basal sheared diamictite (Dm-sh) facies (Fig. 11C) but passes upward into a 1.34-m-thick, diatom-rich mudstone with clasts (Mc/Mdo) that is deformed and physically intermixed in the upper 60 cm with massive diamictite (Dm) and mudstone (Mm) associated with the GSE of overlying Cycle 2 (Figs. 11B and 11C). The age of the diatom-rich mudstone is constrained to between 14.2 Ma and 13.6 Ma (Fig. 2; Table 2).

Depositional setting. The basal contact of each cycle in Facies Succession A contains multiple sedimentary structures that are consistent with the definition of a GSE and overriding by a grounded ice sheet during glacial advance (Figs. 10 and 11). The GSE at the base of Cycle 3 coincides with a high-amplitude seismic reflector that shows a deeply incised channel less than 1 km to the NW of Site U1521, which is consistent with tunnel valleys that form due to the presence of subglacial meltwater within channels beneath grounded ice (Ó Cofaigh, 1996; Gulick, Shevenell, et al., 2017; Fig. 3). The GSE at the base of Cycle 3 also coincides with the seismic boundary RSU 4, which is a highly truncated, erosive surface previously dated to between 15.9 Ma and 14.2 Ma (Figs. 2 and 3; Pérez et al., 2022a). The FAD ages of diatoms in the Dm-sh facies overlying this hiatus and the reverse polarity of this interval indicate that the ice sheet was overriding and eroding preexisting marine strata of 14.48 Ma (or younger) in age, which is consistent with deposition in either chrons C5ACr (14.163–14.07 Ma) or C5ABr (13.739–13.608 Ma). Therefore, the erosion event associated with the RSU4 surface (as recorded by the advance associated with Cycle 3) at Site U1521 postdates 14.163 Ma, but predates 13.608 Ma, due to the absence of the FAD of *Nitzschia denticuloides* in the DO facies at the top of Cycle 3.

The homogeneous nature of the diamictite grain size frequencies with a fine silt mode throughout Facies Succession A are consistent with those of LGM deposits of subglacially deposited till on the topsets of grounding zone wedges in the Ross Sea (Fig. 4; Prothro et al., 2020). Where recovered, glacial retreat facies (Ds and Mc) are relatively thin (<1 m), diatom-rich mudstones and diatomites, which indicate intervals of maximum glacial retreat (Fig. 10) in an arid, terrigenous sediment-starved polar environment similar to the modern Ross Sea (Dunbar et al., 1985; Simkins et al., 2017; Prothro et al., 2018). Glacial minima in cycles 1 and 2 are indicated by diatomites (DO), but Cycle 3 contains more mud (diatom-rich mudstones; Mdo), which suggests that this older cycle of advance and retreat deposited within the MMCT (ca. 14.2–13.6 Ma) may have received turbid meltwater or glaciofluvial runoff, in contrast to Plio-Pleistocene cycles 2 and 1. This is consistent with the evidence of meltwater channel incisions at the base of Cycle 3 (100 ms is equivalent to ~100 m assuming a velocity of 2 km/s twt), which characterizes RSU4 on the seismic profile (Fig. 3).

Large age gaps of several million years between each cycle in the package of Facies Succession A at Site U1521 indicate that the cycles are highly truncated due to extensive glacial overriding and erosion.

DISCUSSION

The five facies successions are grouped into seven distinct packages at Site U1521 (Fig. 2), and each package is interpreted to reflect a major shift in one or more of the following controls: (1) climate, which determines the glacial thermal regime, amount of meltwater, and sedimentation rate; (2) accommodation on the shelf; and (3) grounding-line proximity since the early Miocene. Here, we discuss how the occurrence of each package and facies succession relates to the regional stratigraphic architecture of the margin interpreted from seismic reflection profiles, and regional and global climate controls. We summarize these relationships conceptually in Figure 12.

Early Miocene Aggradational Glacimarine Deposition

The deposition of a package of bioturbated, but otherwise massive, diamictites within Facies Succession E during the earliest Miocene (>17.8 Ma) is interpreted as representing a prolonged interval of glacimarine deposition with minimal grounding-line variance near Site U1521 (Fig. 12). Seismic surveys show that this package consists of aggradational strata beneath seismic surface RSU5 (De Santis et al., 1995; Pérez et al., 2022a), a surface that can be traced to the U2 disconformity in the coastal AND-2A site (Fig. 1), where it is interpreted to represent ice advance beyond the Transantarctic Mountains front (Levy et al., 2016; Pérez et al., 2022b). Sediments underlying this disconformity at AND-2A include an ~100-m-thick package of glacimarine mudstones with clasts that are interpreted to reflect deposition beneath fringing ice shelves along the coastal margin of the western Ross Sea, but not an overriding ice sheet (Levy et al., 2016). Although the homogeneous nature of the diamictite in this interval of U1521 could obscure the identification of GSEs, possible bioturbation in the Dm facies at Site U1521 and the correlation to AND-2A facies suggest that grounded ice was restricted to the inner shelf at this time. Morainal bank complexes emplaced to the south and west of the site at this time are consistent with a tidewater-style ice sheet or caps derived from the terrestrial hinterland landward of the site in both East and West Antarctica (Pérez et al., 2022a).

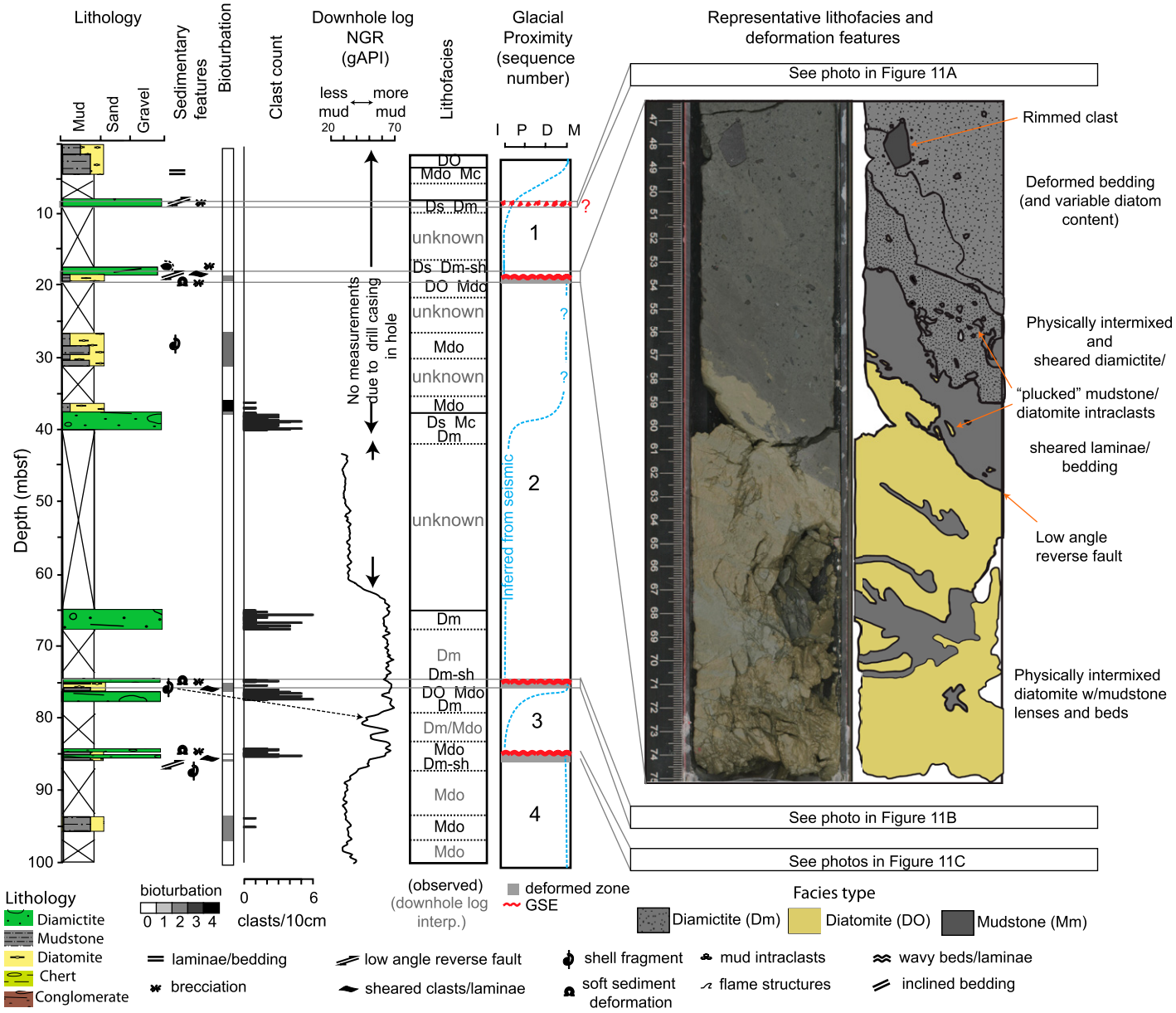

Figure 10. Stratigraphy of Facies Succession A cycles in the 100–0 m below sea floor (mbsf) interval of Site U1521 (cores 1R–11R). From left to right: Lithology (showing intervals of missing recovery); sedimentary features; bioturbation intensity; clast abundance; downhole log natural gamma radiation (NGR, which is wireline log-matched depth below seafloor [WMSF] and likely offset from cores presented on the mbsf depth scale, as recovered core could be placed anywhere in the 9.5 m core run); lithofacies; cycle numbers with glacial proximity curve (blue line; I—ice contact, P—ice proximal, D—ice distal, M—open marine), and glacial surface of erosion sequence boundaries (GSE; red wavy line), with zones of deformation (gray); example photograph of glacial surface of erosion and deformation at 19.03 mbsf (core 3R-2); and locations of core photos in Figure 11. Note: NGR and seismic survey data (Fig. 3) are used to interpret missing core section. Mdo—diatom-rich mudstone; sh—sheared diamictite; Ds—stratified diamictite; Mc—mudstone with clasts.

The aggradational nature of the strata (Fig. 3) is interpreted to represent active accommodation creation during deposition, which facilitated continuous accumulation of glacimarine sediment, whereby the rate of tectonic thermal subsidence exceeds the rate of sediment infilling (Fig. 12). This interpretation is consistent with evidence of late Oligocene to early Miocene regional subsidence in the Ross Sea from Deep Sea Drilling Project (DSDP) Site 270 (Barrett, 1975; Leckie and Webb, 1983; Barrett et al., 1987; De Santis et al., 1995; Wilson and Luyendyk, 2009; Kulhanek et al., 2019; Duncan et al., 2022) and the Cape Roberts Project (Cape Roberts Science Team, 2000; De Santis et al., 2001; Fielding et al., 2008). Uncertainty remains as to whether earlier Miocene advances, such as the Mi-1 event (Duncan et al., 2022), overrode Site U1521, as our record does not date back this far. Notwithstanding this, the deep continental shelf setting (~500 m) of Site U1521 by ca. 18 Ma (Leckie and Webb, 1983; Kulhanek et al., 2019; Duncan et al., 2022; this study) appears to be a key factor in precluding the development of a

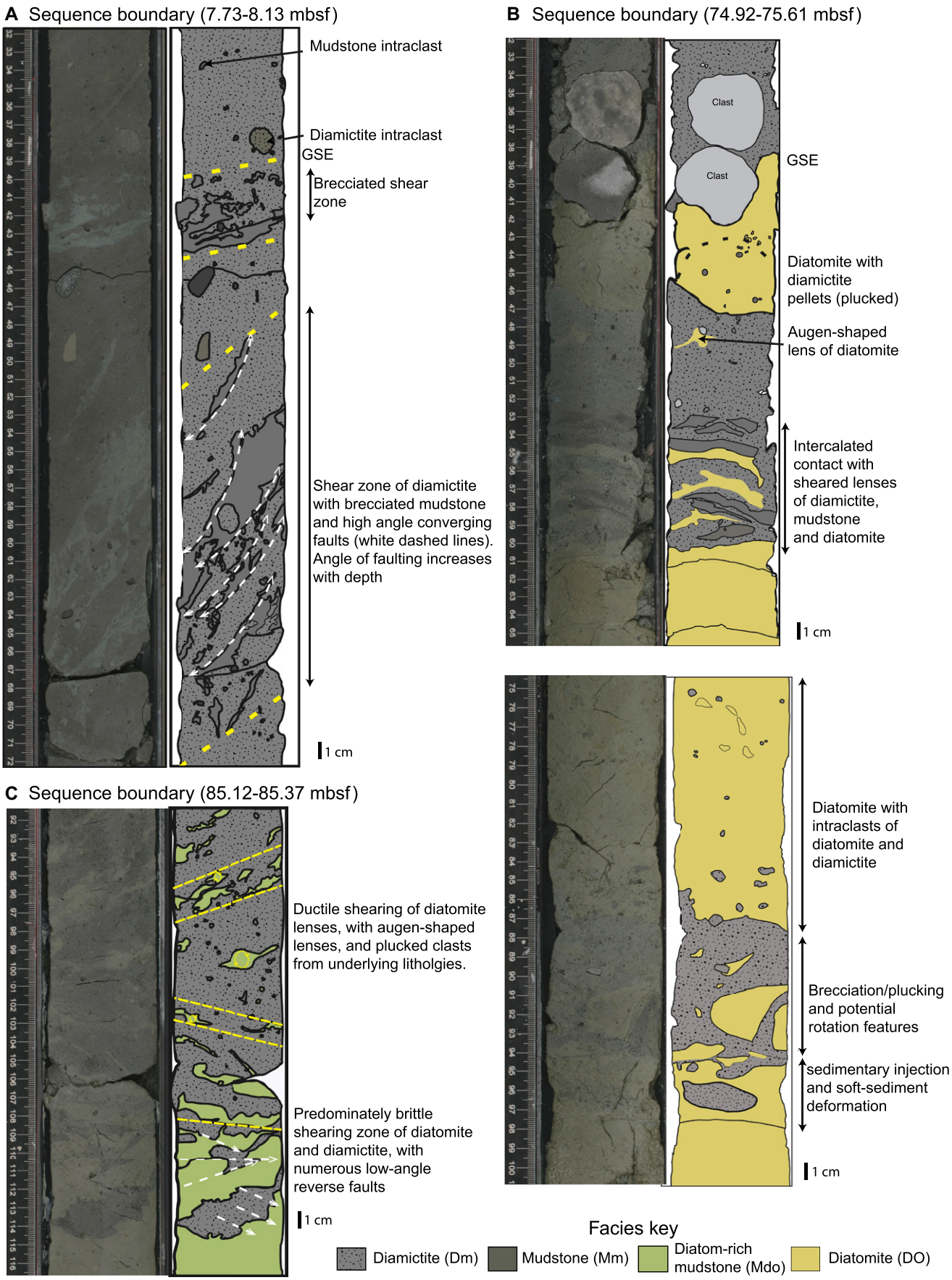

Figure 11. Close-up of interpreted glacial surfaces of erosion (GSE) and associated deformational features in the upper 86 m of the Site U1521. (A) Sheared diamictites and mudstones between 8.13 m below sea floor (mbsf) and 7.73 mbsf (core 2R-1). (B) Sheared diamictite facies and deformed diatomite between 75.61 mbsf and 74.92 mbsf. (Core 9R-1; note: photo is cropped into two sections to show key deformational features.) (C) Sheared diamictite and diatom-rich mudstone facies between 85.37 mbsf and 85.12 mbsf (core 10R-1).

large, marine-based Antarctic Ice Sheet extending to the outermost continental shelf during the deposition of Facies Succession E cycles.

Early Miocene Marine Ice Sheet Advance (17.8–17.4 Ma) with Progradation

The massive to stratified diamictites with thin mudstone beds of Facies Succession D deposited between 17.8 Ma and 17.4 Ma are interpreted to reflect glacimarine deposition in a progradational glacial fan/delta system associated with an expanded marine ice sheet margin, with a lack of evidence of glacial overriding (Fig. 12). This interpretation is supported by the seismic evidence of progradational wedges and rapid infilling of accommodation (~190 m based on clinoform heights) on the outer continental shelf (De Santis et al., 1995; McKay et al., 2019; Pérez et al., 2022a; Fig. 3). Ice advances over the site would also result in highly truncated sequences, which are not observed in seismic profiles or in the Site U1521 age model associated with this Facies Succession D package (Pérez et al., 2022a; Marschalek et al., 2021).

The rapid supply of terrigenous sediment is associated with detrital neodymium isotope values that imply high detrital input from an expanded West Antarctic Ice Sheet between 17.8 Ma and 17.4 Ma (Marschalek et al., 2021). The presence of four cycles capped by mudstone facies implies at least four lulls in proximal glacimarine sediment supply (Figs. 2 and 5) over an ~400 k.y. period, which suggests eccentricity-paced (100 k.y.) fluctuations of the grounding line superimposed on a longer-duration (400 k.y.) continental-scale expansion of West and East Antarctic Ice Sheet glaciation between 17.8 Ma and 17.4 Ma. On land, the rapid glacimarine sedimentation at Site U1521 coincides with onshore records of erosional downcutting by wet-based glaciers and glacifluvial systems in the Transantarctic Mountains (Sugden and Denton, 2004; Pérez et al., 2022b) and West Antarctic Ice Sheet (Marschalek et al., 2021).

We interpret Facies Succession D and its progradational pattern as a phase of ice expansion whereby the rate of sedimentation exceeded the rate of subsidence (Fig. 12), and therefore a slowing or cessation of long-term subsidence. Such an interpretation is supported by evidence of slowing subsidence by 17 Ma at the Cape Roberts Project site in the Western Ross Sea (Cape Roberts Science Team, 2000; Fielding et al., 2008).

Glacimarine Deposition Leading into Onset of the Early Miocene Climate Optimum (17 Ma)

The progradation and rapid infilling of the Facies Succession D package between 17.8 Ma and 17.4 Ma shoaled the outer Ross Sea continental shelf by at least 190 m at Site U1521, with previous seismic isopach mapping indicating an infilling of 175,526 ± 17,553 km^3 of sediment on the outer Ross Sea continental shelf (Marschalek et al., 2021). In the preferred age model solution, the lowest package of Facies Succession C at Site U1521 occurs at ca. 17.2 Ma. This implies a 200 k.y. hiatus from the underlying strata that is potentially due to erosion, or a shift in the sedimentary depocenter of the basin, both of which could have resulted from a changing ice sheet cover. An ice sheet advance over Site U1521 could have led to the deposition of subglacial till sheets during the shift toward aggradation (Pérez et al., 2022a). However, this contrasts with the provenance shift at 17.2 Ma, whereby there is a decreased influence from West Antarctic sources, which suggests a smaller ice sheet in the Ross Sea region (Marschalek et al., 2021). We favor the second scenario, whereby the shift toward aggradational strata that is apparent in the seismic profiles (Fig. 3) represents either (1) migration of the sediment source (e.g., ice sheet grounding line) inland, much in the same way that landward migration of a shoreline results in an onlapping transgressive surface in non-glaciated margin sequence stratigraphy (Catuneanu et al., 2009; Fig. 12); or (2) a shift in direction of the pattern of progradation from a southern source (e.g., West Antarctic Ice Sheet) toward a western source (e.g., East Antarctic Ice Sheet).

Regardless of whether grounded ice overrode Site U1521 or not, the occurrence of grounding-line–proximal facies in the Facies Succession C package between 379.82 mbsf and 324.15 mbsf suggests that large marine-terminating ice sheets were present in the Ross Sea between 17.2 Ma and 17.0 Ma (or ca. 16.72 Ma and 16.54 Ma if the alternate age model solution is used). However, the presence of diatoms (or cherts) and thinner diamictite intervals conforms with the interpretation that despite the ongoing presence of marine-terminating glaciers and ice sheets, ice volumes were reduced in the Ross Sea by 17.2 Ma, as compared to the underlying interval (Marschalek et al., 2021).

A period marked by ice distal to open-water warming is represented by a package of interbedded chertified mudstone (Mch) in the lower package of Facies Succession B (324.15–285.30 mbsf; Fig. 2). In the preferred age model of Marschalek et al. (2021), the age of the base of this interval is interpreted to have been deposited within Chron C5Cr (ca. 17.24 Ma and 16.72 Ma), and a linear interpolation of the age model suggests that the onset of this widespread ice sheet retreat occurred during a period of warmth at the onset of the MCO (Fig. 2). Sea-level estimates (Miller et al., 2020) suggest an initial rise in sea level of ~60 m at the onset of the MCO, and the transition from Facies Succession C to B at 324.15 mbsf provides direct evidence that substantial retreat of a widespread marine-terminating ice sheet toward its terrestrial margin was associated with this sea-level change.

Conglomerate facies (Clc and CLi) identified at the base of each package of Facies Succession C suggest a setting proximal to the grounding line (Figs. 7 and 8A). However, there is a lack of conclusive GSEs, while provenance indicators suggest that these ice sheets were smaller than the large West and East Antarctic Ice Sheet advances between 17.8 Ma and 17.4 Ma (Marschalek et al., 2021). Consequently, it is uncertain whether glacial overriding occurred in these intervals; but regardless, these conglomerates are interpreted to have been deposited in a setting proximal to the grounding line. The depositional setting of Facies Succession C cycles suggests that extensive marine-terminating ice sheets did periodically advance and retreat across the mid-Ross Sea continental shelf during colder intervals of the early MCO between ca. 16.303 Ma and 16.268 Ma (e.g., within Chron C5Cn.1r).

Although 16.3–16.27 Ma represents a period of relative cooling within the MCO, deep-sea isotopes and temperature proxies suggest that it was still warmer than most interglacial Miocene climates between 23 Ma and 17 Ma (Steinthorsdottir et al., 2021; Fig. 2). In this context, the interpretation of Facies Succession C representing marine-terminating ice sheets near the outer continental shelf edge of the Ross Sea during the MCO is a surprising result. However, we have shown that 300 m of sediment infilling occurred between 17.8 Ma and 17.2 Ma. This infilling, with reduced

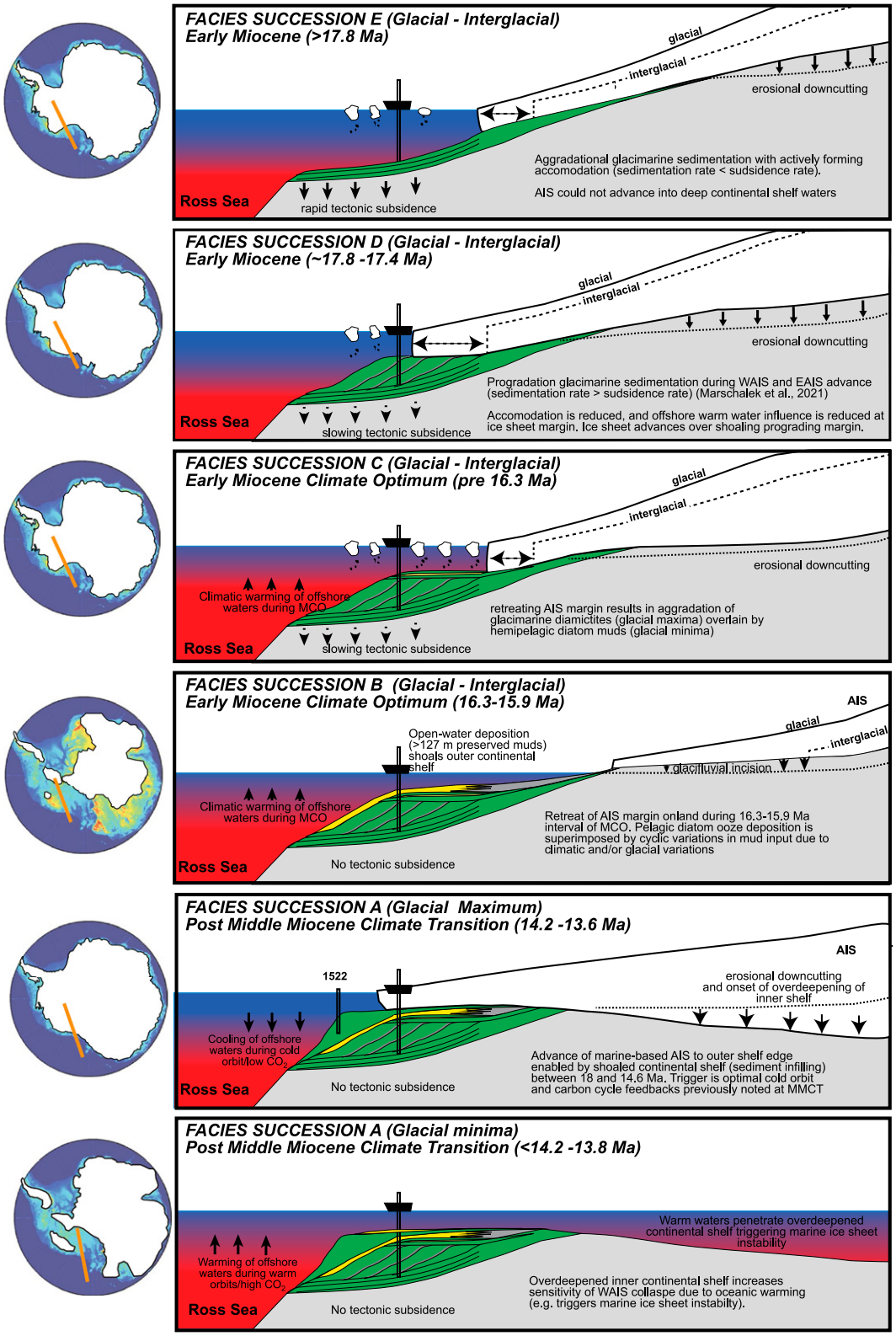

Figure 12. Left column: Maps showing proposed ice sheet extent and reconstructed topography modified from Levy et al. (2019). Right column: Conceptual depositional models for each facies succession along an idealized flowline shown as an orange line in left column maps. Green lithologies represent diamictite-rich facies, gray represents mudstone facies, and yellow represents diatom-rich facies. From top to bottom: Facies Succession E aggradational glacimarine diamictites deposited from marine-terminating ice sheets on a rapidly subsiding continental shelf. Facies Succession D cycles represent widespread West Antarctic Ice Sheet (WAIS) and East Antarctic Ice Sheet (EAIS) expansion between 17.8 Ma and 17.4 Ma forming thick progradational diamictite glacimarine foresets on a subsiding continental shelf during glacial maxima, with thin mudstone intervals deposited during periods of reduced ice sheet extent. Facies Succession C (diatom-rich mudstones interbedded with diamictites) represents cyclic glacimarine advances and retreat during cool intervals of Miocene Climate Optimum (MCO), with a grounding line proximal at peak glacial times, but with no definitive evidence of glacial overriding. Facies Succession B (diatom-rich mudstone) cycles deposited as ice sheets retreated to terrestrial margin during peak MCO warm intervals, with variable terrigenous content relating to interglacial/glacial variance of glacifluvial or glacimarine outwash. Facies Succession A (glacial) diamictites with basal glacial surfaces of erosion represent marine-based ice sheet advance and extensive inland erosion. Facies Succession A (interglacial) diatomites result from widespread marine Antarctic Ice Sheet (AIS) retreat on overdeepened continental shelf in hyper-arid polar setting.

subsidence post-17 Ma, resulted in a significant shoaling of the continental shelf. Consequently, the reduced water column thickness at the ice sheet margin would have reduced the net oceanic heat flux onto the continental shelf, which is a critical control for the melting of marine-based ice sheet margins (Pollard and DeConto, 2009; Golledge et al., 2012). Such a rapid shoaling scenario would allow the margins of predominantly terrestrial ice

sheets to periodically readvance across the shallower continental shelf regions during the cold periods of the MCO (Fig. 12).

Benthic foraminiferal $\delta^{18}O$-based sea-level estimates (Miller et al., 2020) show ~40 m variations within the MCO, which accounts for the ice sheet re-advance demonstrated by the Facies Succession C cycles (Fig. 2). Notably, the deep-sea $\delta^{18}O$ record indicates a period of relative warmth and reduced ice volume at the onset of the upper package of Facies Succession C at 16.3 Ma (Fig. 2). Advance of a predominantly terrestrial East Antarctic Ice Sheet could have been triggered by oceanic warming that resulted in enhanced coastal precipitation, which is a process previously proposed by Shevenell et al. (2004, 2008) and observed in Miocene ice sheet model experiments (Halberstadt et al., 2021). However, such warmth would restrict the development of extensive marine-based ice sheets onto deeper portions of the outermost continental shelves due to the enhanced oceanic heat flux (Pollard and DeConto, 2009; Golledge et al., 2012, 2017). Consequently, we propose that the expansion of a predominantly terrestrial ice sheet into the marine continental margin proximal to Site U1521 in these warmer climates was enabled by the extensive shoaling of the outer continental shelf during the preceding intervals of rapid glacimarine sedimentation, rather than climate forcings alone (Fig. 12).

Peak Retreat of Marine-Terminating Ice during the Early Miocene Climate Optimum

Between ca. 16.3 Ma and 15.95 Ma, Site U1521 contains 123 m of diatom-bearing mudstone to diatomite (Facies Succession B) subcycles (Fig. 2). These sub-cycles indicate a variable, yet decreasing, supply of terrigenous sediment on the background of a prolonged interval of open-marine, low-energy hemipelagic deposition. The lack of coarse glacimarine sediment and ice-rafted debris (IRD; Fig. 2) implies that regional ice sheets may have been predominantly terrestrial through this interval (Fig. 12). Variations in terrigenous sediment supply likely resulted from changes in terrestrial runoff (e.g., turbid meltwater) from glacifluvial systems, and suggest that surface melt strongly influenced East Antarctic Ice Sheet mass balance. Indeed, stratigraphic data from landward Site AND-2A (Levy et al., 2016), and high-elevation outcrops in the Transantarctic Mountains, indicate that reduced East Antarctic Ice Sheet extent, extensive wet-based glacial regimes, and expansive glacifluvial systems in the Dry Valleys persisted until at least 14.2 Ma (Sugden and Denton, 2004; Lewis et al., 2006, 2007, 2008; Chorley et al., 2022).

The snapshot of peak ice retreat from 16.3 Ma to 15.95 Ma preserved at Site U1521 also coincides with high sea levels and Southern Ocean warmth (Shevenell et al., 2004, 2008; Miller et al., 2020; Fig. 2). Although atmospheric pCO_2 reconstructions have large uncertainties, the latest compilations display sustained values exceeding 500 ppm in boron-based reconstructions and 350 ppm in alkenone-based reconstructions ($CenCO_2PIP$ Consortium, 2023) during this period (Fig. 2). The lack of IRD and mudstone variations in Facies Succession B suggests that under a state of climatic equilibrium, significant surface melt and retreat of the East Antarctic Ice Sheet may have occurred within this range of atmospheric pCO_2.

Marine Ice Sheet Expansion during the Mid-Miocene Climate Transition

The ca. 15.95–14.2 Ma interval of the MCO is missing at Site U1521, due to erosion associated with the RSU4 seismic surface (Fig. 3). The benthic foraminifer $\delta^{18}O$ isotope record suggests a large (>40 m) sea-level fall at 15.95 Ma (John et al., 2011; Miller et al., 2020). This is consistent with our evidence of pre-16.3 Ma marine ice sheet advances proximal to Site U1521 (e.g., Facies Succession C intervals), which indicates that ice sheet advances in the later MCO were also likely. However, thick packages of conformable strata immediately overlying the diatom-rich mudstones of Facies Succession B (Fig. 3) occur to the east of Site U1521, so it remains unclear whether mid- to outer continental shelf ice sheet overriding occurred in the Ross Sea between 15.95 Ma and 14.2 Ma (Figs. 2 and 12).

The MMCT is defined in proxy records as a long-term trend toward increasing $\delta^{18}O$ values in deep-sea benthic foraminiferal records after ca. 14.2 Ma, an inferred drop in sea level of ~60 m (Miller et al., 2020), and a shift to lower pCO_2 values based on proxy estimates ($CenCO_2PIP$ Consortium, 2023; Fig. 2). Overlying the RSU4 erosion surface at Site U1521 are Facies Succession A cycles, which contain unequivocal GSEs at the base of each cycle (Fig. 11). The lowermost cycle, which resulted in erosion of the 15.95–14.2 Ma interval, has a deposition date of between 14.2 Ma and 13.6 Ma (Figs. 2 and 3). This provides the first direct, well-dated evidence of an ice sheet overriding the outer continental shelf during the onset of the MMCT, an event larger in extent than any of the prior ice sheet advances between 18 Ma and 14.2 Ma (Fig. 12).

At the top of this lowermost Facies Succession A cycle at Site U1521, a thick, muddy diatomite was deposited sometime between 14.2 Ma and 13.6 Ma. This indicates that despite periods of full continental shelf Antarctic Ice Sheet advance, regional ice did periodically retreat within interglacials of the MMCT (Fig. 2). Diatom content in this ~1.5-m-thick interval is higher than in the diatom-rich mudstones in the Facies Succession B cycles (McKay et al., 2019), while the transition from subglacial glacimarine diamictites is sharp (Fig. 10). As noted in the Background Section of the Introduction, previous facies models show that such sediment starvation is indicative of reduced turbid glacial meltwater input due to ice sheet mass balance controls becoming increasingly dominated by basal melting of floating ice shelf margins, frontal melting of tidewater systems, and iceberg calving, rather than extensive surface melting. This is also consistent with geomorphological and sedimentary facies evidence in the Transantarctic Mountains that shows a shift toward cold-based mountain glaciation, hyper-aridity in the McMurdo Dry Valleys, and decreased subglacial outburst floods after 13.6 Ma (Sugden and Denton, 2004; Lewis et al., 2006, 2007, 2008; Pérez et al., 2022b). Although turbid meltwater was greatly reduced after 13.6 Ma, we note that previous studies have shown that some turbid meltwater processes did persist in coastal regions around the East Antarctic Ice Sheet until the late Miocene (McKay et al., 2009; Rosenblume and Powell, 2019; Hambrey and McKelvey, 2000; Whitehead et al., 2004; Gulick, Shevenell, et al., 2017).

Late Miocene to Present

A late Miocene/early Pliocene advance/retreat cycle and the LGM to recent retreat cycle are preserved in the stratigraphy at Site U1521, with the basal erosion surface of these cycles also clearly evident in the seismic stratigraphy (Figs. 3 and 10). Seismic profiles also show that extensive shelf margin progradation shifted into the Eastern Basin (Fig. 2) after RSU4, which supports earlier studies that indicate this inland sediment erosion from major ice sheet advance between the MMCT and the early Pliocene resulted in extensive overdeepening of the inner continental shelf (De Santis et al., 1995; Bart, 2001; Kim et al., 2018; McKay et al., 2019, 2022b). AND-1B also preserved at least 38 ice retreat events in the Plio-Pleistocene (Naish et al., 2009) that are not preserved at Site U1521 (Fig. 12). Overdeepening of the inner continental shelf by these repetitive advances of marine-based Antarctic Ice Sheet in the cooler climates since the MMCT would ultimately act to counteract some of the sediment infilling feedbacks we propose for the MCO. However, the combined influence

of the erosion and deepening of the inner shelf, alongside shoaling of the outer shelf, would amplify the reverse slope gradient of the continental shelf. Such a configuration enhances the potential for threshold behavior of the West Antarctic Ice Sheet via marine ice sheet instability processes by Pliocene times (Bart et al., 2016; Colleoni et al., 2018). The uppermost Facies Succession A cycle at Site U1521 likely reflects ice retreat during the last deglaciation, as a similar stratigraphy is preserved in a series of sediment cores in close proximity to the site (Salvi et al., 2006; Prothro et al., 2020).

CONCLUSIONS

The stratigraphy of IODP Site U1521 provides unique insight into the variability of continental-scale ice sheets over the MCO and MMCT. Several hypotheses exist to explain the ice growth at the MMCT, including changes in carbon cycling (Zachos et al., 2001; Super et al., 2018; Sosdian et al., 2018; Rae et al., 2021; Cen-CO_2PIP Consortium, 2023), the meridional heat flux to Antarctica (Kennett, 1977; Flower and Kennett, 1994; Shevenell et al., 2004, 2008), and an orbital configuration that is conducive to ice growth (Holbourn et al., 2005, 2007).

While such forcing mechanisms would have contributed to the state of the background climate and regulated the thresholds under which the Antarctic Ice Sheet grew or decayed (DeConto et al., 2008), our results show that local geological forcings played an equally fundamental role in regulating the growth and decay of marine-terminating ice sheets in the Ross Sea during the MCO and MMCT.

(1) Prior to 18 Ma, ongoing tectonic subsidence in the outer Ross Sea is demonstrated by the aggradational pattern of glacimarine diamictites (Facies Succession E). This subsidence restricted the growth of marine-based ice sheets onto the relatively deep outer continental shelf.

(2) By ca. 17.8 Ma, the rate of sedimentation began to outpace subsidence, resulting in a shift of deposition to progradational strata between 17.8 Ma and 17.4 Ma. Rapid emplacement of glacimarine diamictites and mudstones (Facies Succession D) from a major glacial advance in West Antarctica (Marschalek et al., 2021) resulted in a shoaling of the outer continental shelf of ~190 m at Site U521 over this time.

(3) Alternations of glacimarine diamictites/diatom-rich mudstone (Facies Succession C) and thick sequences of hemipelagic diatom-rich mudstones (Facies Succession B) during the early MCO suggest that although widespread retreat of the Antarctic Ice Sheet on land occurred during peak warmth of the MCO, widespread marine glaciation occurred during cold intervals of the MCO. This is the first direct evidence of extensive variability in ice sheet volume during the MCO, and helps explain far-field sea-level records showing more than 20 m of sea-level variability (Miller et al., 2020).

(4) The combination of highly productive surface waters, turbid meltwater run-off during peak warm intervals of the MCO, and periodic glacimarine sediment supply during glacials of the MCO allowed for deposition of another ~300 m of diamictite and diatom-rich mudstone between 17.4 Ma and 15.9 Ma (Fig. 12).

(5) Facies Succession A cycles at Site U1521 provide the first direct evidence of continental shelf-wide expansion of the Antarctic Ice Sheet across the Ross Sea at the MMCT, a hypothesis previously only inferred from inland studies, deep-sea isotopes, or poorly dated seismic interpretations. We hypothesize that shoaling related to slowing tectonic subsidence with infilling of up to 590 m of sediment between 18 Ma and 14.2 Ma allowed the advance of marine-terminating glaciers at the MMCT beyond the limits of previous ice advances. Past advances were either restricted due to a deeper, actively subsiding shelf environment or global warmth during the early MCO. Furthermore, a shallower continental shelf may have restricted warm intermediate water masses (e.g., Northern Component Water and/or Tethyan Indian Saline Water) from reaching the Ross Sea continental shelf. This would have further reduced oceanic heat flux to Antarctica, resulting in ice expansion, and increased regional aridity since the late MCO and MMCT (Fig. 12).

While the local boundary conditions were different in the MCO with a shallower continental shelf, our study also indicates that the sustained high atmospheric pCO_2 levels of the MCO not only resulted in loss of the marine-based Antarctic Ice Sheet margin, but also triggered substantial surface melting of the East Antarctic Ice Sheet. Importantly, the shoaling of the outer continental shelf combined with extensive overdeepening of Antarctica's inner continental shelves have only acted to increase the potential for threshold behavior in marine-based ice sheet sectors since the MMCT, via marine ice sheet instability processes that operate on reverse slope continental shelves. This is concerning for the modern ice sheets, as atmospheric pCO_2 concentrations and southern high-latitude atmospheric/oceanic temperatures rise back to levels not seen since the Miocene.

ACKNOWLEDGMENTS

This research used data and samples provided by the International Ocean Discovery Program (IODP), which is sponsored by the U.S. National Science Foundation (NSF), the European Consortium for Ocean Research Drilling (ECORD), and participating countries under the management of the Joint Oceanographic Institutions. R. McKay, B. Duncan, G. Cortese, J. Cockrell, and J. Burns were funded by Marsden Grant Fund 18-VUW-089. R. McKay, R. Levy, B. Duncan, and T. Naish were supported by the New Zealand Ministry of Business, Innovation and Employment Antarctic Science Platform (ANTA1801). The IHS-Kingdom project was supported through academic licenses released to the National Institute of Oceanography and Applied Geophysics (Trieste, Italy). L. De Santis's funding was provided by the Italian National Antarctic Research Program (PNRA16_00016 project). A. Shevenell and I. Browne were supported by U.S. Science Support Program Post Expedition Awards and National Science Foundation OPP ANT #1947646 to A. Shevenell, M. Leckie, and J. Dodd. L. Pérez was funded through the European Union's Horizon 2020 research and innovation program under the Marie Sklodowska-Curie grant agreement number 792773. M. Patterson, B. Romans, and D. Kulhanek were supported by National Science Foundation awards OPP-2000995, OPP-2000997 and OPP-2000992. T. van de Flierdt and J. Marschalek were funded through Natural Environment Research Council grants NE/R018219/1 and NE/W000172/1. J.S. Laberg was supported by the European Consortium for Ocean Research Drilling (ECORD) and the Research Council of Norway. We thank the two anonymous reviewers, associate editor, and science editor for providing constructive feedback that improved the paper. All data are available in the Supplemental Material[1] or in the IODP data repository (https://zenodo.org/communities/iodp) cited in McKay et al. (2019).

REFERENCES CITED

Anderson, J.B., and Bartek, L.R., 1992, Cenozoic glacial history of the Ross Sea revealed by intermediate resolution seismic reflection data combined with drill site information, *in* Kennett, J.P., and Warkne, D.A., eds., The Antarctic Paleoenvironment: A Perspective on Global Change: Part One: Washington, D.C., American Geophysical Union, Antarctic Research Series, v. 56, p. 231–264, https://doi.org/10.1029/AR056p0231.

Arndt, J.E., et al., 2013, The International Bathymetric Chart of the Southern Ocean (IBCSO) Version 1.0—A new bathymetric compilation covering circum-Antarctic waters: Geophysical Research Letters, v. 40, p. 3111–3117, https://doi.org/10.1002/grl.50413.

Barrett, P.J., 1975, Textural characteristics of Cenozoic preglacial and glacial sediments at site 270, Ross Sea, Antarctica, *in* Hayes et al., eds., Initial Reports of the Deep Sea Drilling Project 28: Washington, D.C., U.S Government Printing Office, p. 757–767, https://doi.org/10.2973/dsdp.proc.28.122.1975.

Barrett, P.J., 1989, Antarctic Cenozoic History from the CIROS-1 Drillhole, McMurdo Sound: DSIR Publishing, DSIR Bulletin 245, 254 p.

Barrett, P.J., Elston, D.P., Harwood, D.M., McKelvey, B.C., and Webb, P.N., 1987, Mid-Cenozoic record of glaciation and sea-level change on the margin of the Victoria Land basin, Antarctica: Geology, v. 15, p. 634–637, https://doi.org/10.1130/0091-7613(1987)15<634:MROGAS>2.0.CO;2.

Bart, P.J., 2001, Did the Antarctic Ice Sheets expand during the early Pliocene?: Geology, v. 29, p. 67–70, https://doi.org/10.1130/0091-7613(2001)029<0067:DTAntarctic Ice SheetE>2.0.CO;2.

[1]Supplemental Material. Grain size data for IODP Site U1521. Please visit https://doi.org/10.1130/GSAB.S.27018574 to access the supplemental material; contact editing@geosociety.org with any questions.

Bart, P.J., 2003, Were West Antarctic Ice Sheet grounding events in the Ross Sea a consequence of East Antarctic Ice Sheet expansion during the middle Miocene?: Earth and Planetary Science Letters, v. 216, p. 93–107, https://doi.org/10.1016/S0012-821X(03)00509-0.

Bart, P.J., Mullally, D., and Golledge, N.R., 2016, The influence of continental shelf bathymetry on Antarctic Ice Sheet response to climate forcing: Global and Planetary Change, v. 142, p. 87–95, https://doi.org/10.1016/j.gloplacha.2016.04.009.

Boulton, G.S., Dobbie, K.E., and Zatsepin, S., 2001, Sediment deformation beneath glaciers and its coupling to the subglacial hydraulic system: Quaternary International, v. 86, p. 3–28, https://doi.org/10.1016/S1040-6182(01)00048-9.

Boyce, J.I., and Eyles, N., 2000, Architectural element analysis applied to glacial deposits: Internal geometry of a late Pleistocene till sheet, Ontario, Canada: Geological Society of America Bulletin, v. 112, p. 98–118, https://doi.org/10.1130/0016-7606(2000)112<98:AEAATG>2.0.CO;2.

Brancolini, G., et al., 1995, ANTOSTRAT Project, seismic stratigraphic atlas of the Ross Sea, Antarctica, *in* Cooper, A.K., Barker, P.F., and Brancolini, G., eds., Geology and Seismic Stratigraphy of the Antarctic Margin: Washington, D.C., American Geophysical Union, Antarctic Research Series, v. 68, p. 209–234.

Cape Roberts Science Team, 2000, Studies from the Cape Roberts Project, Ross Sea, Antarctica: Initial report on CRP-3: Terra Antarctica, v. 7, 209 p.

Carter, A., Riley, T.R., Hillenbrand, C.-D., and Rittner, M., 2017, Widespread Antarctic glaciation during the late Eocene: Earth and Planetary Science Letters, v. 458, p. 49–57, https://doi.org/10.1016/j.epsl.2016.10.045.

Catuneanu, O., et al., 2009, Towards the standardization of sequence stratigraphy: Earth-Science Reviews, v. 92, p. 1–33, https://doi.org/10.1016/j.earscirev.2008.10.003.

CenCO_2PIP Consortium, 2023, Toward a Cenozoic history of atmospheric CO_2: Science, v. 382, https://doi.org/10.1126/science.adi5177.

Chewings, J.M., Atkins, C.B., Dunbar, G.B., and Golledge, N.R., 2014, Aeolian sediment transport and deposition in a modern high-latitude glacial marine environment: Sedimentology, v. 61, p. 1535–1557, https://doi.org/10.1111/sed.12108.

Chorley, H., et al., 2022, East Antarctic Ice Sheet variability during the middle Miocene Climate Transition captured in drill cores from the Friis Hills, Transantarctic Mountains: Geological Society of America Bulletin, v. 135, p. 1503–1529, https://doi.org/10.1130/B36531.1.

Chu, V.W., Smith, L.C., Rennermalm, A.K., Forster, R.R., Box, J.E., and Reeh, N., 2009, Sediment plume response to surface melting and supraglacial lake drainages on the Greenland ice sheet: Journal of Glaciology, v. 55, p. 1072–1082, https://doi.org/10.3189/002214309790794904.

Cody, R.D., Levy, R.H., Harwood, D.M., and Sadler, P.M., 2008, Thinking outside the zone: High-resolution quantitative diatom biochronology for the Antarctic Neogene: Palaeogeography, Palaeoclimatology, Palaeoecology, v. 260, p. 92–121, https://doi.org/10.1016/j.palaeo.2007.08.020.

Colleoni, F., et al., 2018, Past continental shelf evolution increased Antarctic Ice Sheet sensitivity to climatic conditions: Scientific Reports, v. 8, https://doi.org/10.1038/s41598-018-29718-7.

Cooper, A.K., Barrett, P.J., Hinz, K., Traube, V., Letichenkov, G., and Stagg, H.M.J., 1991, Cenozoic prograding sequences of the Antarctic continental margin: A record of glacio-eustatic and tectonic events: Marine Geology, v. 102, p. 175–213, https://doi.org/10.1016/0025-3227(91)90008-R.

Cooper, A.K., Barker, P.F., and Brancolini, G., eds., 1995, Geology and Seismic Stratigraphy of the Antarctic Margin: Washington, D.C., American Geophysical Union, v. 68, 303 p., https://doi.org/10.1029/AR068.

Cooper, A.K., Brancolini, G., Escutia, C., Kristoffersen, Y., Larter, R., Leitchenkov, G., O'Brien, P., and Jokat, W., 2008, Cenozoic climate history from seismic reflection and drilling studies on the Antarctic continental margin, *in* Florindo, F., and Siegert, M., eds., Antarctic Climate Evolution: Elsevier, Developments in Earth and Environmental Sciences, v. 8, p. 115–234, https://doi.org/10.1016/S1571-9197(08)00005-0.

Cowan, E.A., Seramur, K.C., Cai, J., and Powell, R.D., 1999, Cyclic sedimentation produced by fluctuations in meltwater discharge, tides and marine productivity in an Alaskan fjord: Sedimentology, v. 46, p. 1109–1126, https://doi.org/10.1046/j.1365-3091.1999.00267.x.

Cowan, E.A., Christoffersen, P., and Powell, R.D., 2012, Sedimentological signature of a deformable bed preserved beneath an ice stream in a late Pleistocene glacial sequence, Ross Sea, Antarctica: Journal of Sedimentary Research, v. 82, p. 270–282, https://doi.org/10.2110/jsr.2012.25.

Crampton, J.S., Cody, R.D., Levy, R., Harwood, D., McKay, R., and Naish, T.R., 2016, Southern Ocean phytoplankton turnover in response to stepwise Antarctic cooling over the past 15 million years: Proceedings of the National Academy of Sciences of the United States of America, v. 113, p. 6868–6873, https://doi.org/10.1073/pnas.1600318113.

Cui, Y., Schubert, B.A., and Jahren, A.H., 2020, A 23 m.y. record of low atmospheric CO_2: Geology, v. 48, p. 888–892, https://doi.org/10.1130/G47681.1.

DeConto, R.M., and Pollard, D., 2003, Rapid Cenozoic glaciation of Antarctica induced by declining atmospheric CO_2: Nature, v. 421, p. 245–249, https://doi.org/10.1038/nature01290.

DeConto, R.M., Pollard, D., Wilson, P.A., Pälike, H., Lear, C.H., and Pagani, M., 2008, Thresholds for Cenozoic bipolar glaciation: Nature, v. 455, p. 652–656, https://doi.org/10.1038/nature07337.

Depoorter, M.A., Bamber, J.L., Griggs, J.A., Lenaerts, J.T.M., Ligtenberg, S.R.M., van den Broeke, M.R., and Moholdt, G., 2013, Calving fluxes and basal melt rates of Antarctic ice shelves: Nature, v. 502, p. 89–92, https://doi.org/10.1038/nature12567.

De Santis, L., Anderson, J.B., Brancolini, G., and Zayatz, I., 1995, Seismic record of late Oligocene through Miocene glaciation on the central and eastern continental shelf of the Ross Sea, *in* Cooper, A.K., Barker, P.F., and Brancolini, G., eds., Geology and Seismic Stratigraphy of the Antarctic Margin: Washington, D.C., American Geophysical Union, Antarctic Research Series, v. 68, p. 235–260, https://doi.org/10.1029/AR068p0235.

De Santis, L., Davey, F., Prato, S., and Brancolini, G., 2001, Subsidence at the Cape Roberts Project (CRP) drillsites from backstripping techniques, Victoria Land Basin, Antarctica: Terra Antarctica, v. 8, p. 137–141.

Domack, E.W., Jacobson, E.A., Shipp, S., and Anderson, J.B., 1999, Late Pleistocene–Holocene retreat of the West Antarctic Ice-Sheet system in the Ross Sea: Part 2—Sedimentologic and stratigraphic signature: Geological Society of America Bulletin, v. 111, p. 1517–1536, https://doi.org/10.1130/0016-7606(1999)111<1517:LPHROT>2.3.CO;2.

Dowdeswell, J.A., Whittington, R.J., and Marienfeld, P., 1994, The origin of massive diamicton facies by iceberg rafting and scouring, Scoresby Sund, East Greenland: Sedimentology, v. 41, p. 21–35, https://doi.org/10.1111/j.1365-3091.1994.tb01390.x.

Dowdeswell, J.A., Elverhfi, A., and Spielhagen, R., 1998, Glacimarine sedimentary processes and facies on the polar North Atlantic margins: Quaternary Science Reviews, v. 17, p. 243–272, https://doi.org/10.1016/S0277-3791(97)00071-1.

Dowdeswell, J.A., Ó Cofaigh, C., Taylor, J., Kenyon, N.H., Mienert, J., and Wilken, M., 2002, On the architecture of high-latitude continental margins: The influence of ice-sheet and sea-ice processes in the Polar North Atlantic, *in* Dowdeswell, J.A., and Ó Cofaigh, C., eds., Glacier-Influenced Sedimentation on High-Latitude Continental Margins: Geological Society, London, Special Publication 203, p. 33–54, https://doi.org/10.1144/GSL.SP.2002.203.01.03.

Dowdeswell, J.A., Hogan, K.A., Arnold, N.S., Mugford, R.I., Wells, M., Hirst, J.P.P., and Decalf, C., 2015, Sediment-rich meltwater plumes and ice-proximal fans at the margins of modern and ancient tidewater glaciers: Observations and modelling: Sedimentology, v. 62, p. 1665–1692, https://doi.org/10.1111/sed.12198.

Dunbar, G.B., and Barrett, P.J., 2005, Estimating palaeobathymetry of wave-graded continental shelves from sediment texture: Sedimentology, v. 52, p. 253–269, https://doi.org/10.1111/j.1365-3091.2004.00695.x.

Dunbar, R.B., Anderson, J.B., Domack, E.W., and Jacobs, S.S., 1985, Oceanographic influences on sedimentation along the Antarctic continental shelf, *in* Jacobs, S.S., ed., Oceanology of the Antarctic Continental Shelf: Washington, D.C., American Geophysical Union, Antarctic Research Series, v. 13, p. 291–312, https://doi.org/10.1029/AR043p0291.

Duncan, B., McKay, R., Levy, R., Naish, T., Prebble, J., Sangiorgi, F., Krishnan, S., Hoem, F., Clowes, C., and Dunkley Jones, T., 2022, Climatic and tectonic drivers of late Oligocene Antarctic ice volume: Nature Geoscience, v. 15, p. 819–825, https://doi.org/10.1038/s41561-022-01025-x.

Escutia, C., Brinkhuis, H., and Expedition 318 Scientists, 2014, From greenhouse to icehouse at the Wilkes Land Antarctic Margin: IODP Expedition 318 synthesis of results, *in* Stein, R., Blackman, D.K., Inagaki, F., and Larsen, H.-C., eds., Developments in Marine Geology: Elsevier, v. 7, p. 295–328, https://doi.org/10.1016/B978-0-444-62617-2.00012-8.

Evans, D.J.A., and Benn, D.I., eds., 2014, A Practical Guide to the Study of Glacial Sediments: Routledge, 297 p., https://doi.org/10.4324/9780203783481.

Feakins, S.J., Warny, S., and Lee, J.-E., 2012, Hydrologic cycling over Antarctica during the middle Miocene warming: Nature Geoscience, v. 5, p. 557–560, https://doi.org/10.1038/ngeo1498.

Fielding, C.R., Naish, T.R., Woolfe, K.J., and Lavelle, M., 2000, Facies analysis and sequence stratigraphy of CRP-2/2A, Victoria Land basin, Antarctica: Terra Antarctica, v. 7, p. 323–338.

Fielding, C.R., Whittaker, J., Henrys, S.A., Wilson, T.J., and Naish, T.R., 2008, Seismic facies and stratigraphy of the Cenozoic succession in McMurdo Sound, Antarctica: Implications for tectonic, climatic and glacial history: Palaeogeography, Palaeoclimatology, Palaeoecology, v. 260, p. 8–29, https://doi.org/10.1016/j.palaeo.2007.08.016.

Florindo, F., Farmer, R.K., Harwood, D.M., Cody, R.D., Levy, R., Bohaty, S.M., Carter, L., and Winkler, A., 2013, Paleomagnetism and biostratigraphy of sediments from Southern Ocean ODP Site 744 (southern Kerguelen Plateau): Implications for early-to-middle Miocene climate in Antarctica: Global and Planetary Change, v. 110, p. 434–454, https://doi.org/10.1016/j.gloplacha.2013.05.004.

Flower, B.P., and Kennett, J.P., 1994, The middle Miocene climatic transition: East Antarctic Ice Sheet development, deep ocean circulation and global carbon cycling: Palaeogeography, Palaeoclimatology, Palaeoecology, v. 108, p. 537–555, https://doi.org/10.1016/0031-0182(94)90251-8.

Galeotti, S., et al., 2016, Antarctic Ice Sheet variability across the Eocene-Oligocene boundary climate transition: Science, v. 352, p. 76–80, https://doi.org/10.1126/science.aab0669.

Gasson, E., DeConto, R.M., Pollard, D., and Levy, R.H., 2016, Dynamic Antarctic Ice Sheet during the early to mid-Miocene: Proceedings of the National Academy of Sciences of the United States of America, v. 113, p. 3459–3464, https://doi.org/10.1073/pnas.1516130113.

Golledge, N.R., Fogwill, C.J., Mackintosh, A.N., and Buckley, K.M., 2012, Dynamics of the last glacial maximum Antarctic ice-sheet and its response to ocean forcing: Proceedings of the National Academy of Sciences, v. 109, p. 16,052–16,056, https://doi.org/10.1073/pnas.1205385109.

Golledge, N.R., et al., 2013, Glaciology and geological signature of the Last Glacial Maximum Antarctic Ice Sheet: Quaternary Science Reviews, v. 78, p. 225–247, https://doi.org/10.1016/j.quascirev.2013.08.011.

Golledge, N.R., Levy, R.H., McKay, R.M., and Naish, T.R., 2017, East Antarctic Ice Sheet most vulnerable to Weddell Sea warming: Geophysical Research Letters, v. 44, p. 2343–2351, https://doi.org/10.1002/2016GL072422.

Greenop, R., Foster, G.L., Wilson, P.A., and Lear, C.H., 2014, Middle Miocene climate instability associ-

ated with high-amplitude CO_2 variability: Paleoceanography, v. 29, p. 845–853, https://doi.org/10.1002/2014PA002653.

Gulick, S.P.S., Shevenell, A.E., et al., 2017, Initiation and long-term instability of the East Antarctic Ice Sheet: Nature, v. 552, p. 225–229, https://doi.org/10.1038/nature25026.

Halberstadt, A.R.W., Chorley, H., Levy, R.H., Naish, T., DeConto, R.M., Gasson, E., and Kowalewski, D.E., 2021, CO_2 and tectonic controls on Antarctic climate and ice-sheet evolution in the mid-Miocene: Earth and Planetary Science Letters, v. 564, https://doi.org/10.1016/j.epsl.2021.116908.

Hambrey, M.J., and McKelvey, B., 2000, Neogene fjordal sedimentation on the western margin of the Lambert Graben, East Antarctica: Sedimentology, v. 47, p. 577–607, https://doi.org/10.1046/j.1365-3091.2000.00308.x.

Hambrey, M.J., Barrett, P.J., Ehrmann, W.U., and Larsen, B., 1992, Cenozoic sedimentary processes on the Antarctic continental margin and the record from deep drilling: Zeitschrift für Geomorphologie, v. 86, Supplementband, p. 77–103.

Holbourn, A., Kuhnt, W., Schulz, M., and Erlenkeuser, H., 2005, Impacts of orbital forcing and atmospheric carbon dioxide on Miocene ice-sheet expansion: Nature, v. 438, p. 483–487, https://doi.org/10.1038/nature04123.

Holbourn, A., Kuhnt, W., Schulz, M., Flores, J.-A., and Andersen, N., 2007, Orbitally-paced climate evolution during the middle Miocene "Monterey" carbon-isotope excursion: Earth and Planetary Science Letters, v. 261, p. 534–550, https://doi.org/10.1016/j.epsl.2007.07.026.

Horgan, H.J., Alley, R.B., Christianson, K., Jacobel, R.W., Anandakrishnan, S., Muto, A., Beem, L.H., and Siegfried, M.R., 2013, Estuaries beneath ice sheets: Geology, v. 41, p. 1159–1162, https://doi.org/10.1130/G34654.1.

Intergovernmental Panel on Climate Change (IPCC), ed., 2022, Polar regions, *in* The Ocean and Cryosphere in a Changing Climate: Special Report of the Intergovernmental Panel on Climate Change: Cambridge, UK, Cambridge University Press, p. 203–320, https://doi.org/10.1017/9781009157964.005.

Jaeger, J.M., and Koppes, M.N., 2016, The role of the cryosphere in source-to-sink systems: Earth-Science Reviews, v. 153, p. 43–76, https://doi.org/10.1016/j.earscirev.2015.09.011.

Ji, F., Li, F., Gao, J.-Y., Zhang, Q., and Hao, W.-F., 2018, 3-D density structure of the Ross Sea basins, West Antarctica from constrained gravity inversion and their tectonic implications: Geophysical Journal International, v. 215, p. 1241–1256, https://doi.org/10.1093/gji/ggy343.

John, C.M., Karner, G.D., Browning, E., Leckie, R.M., Mateo, Z., Carson, B., and Lowery, C., 2011, Timing and magnitude of Miocene eustasy derived from the mixed siliciclastic-carbonate stratigraphic record of the northeastern Australian margin: Earth and Planetary Science Letters, v. 304, p. 455–467, https://doi.org/10.1016/j.epsl.2011.02.013.

Kennett, J.P., 1977, Cenozoic evolution of Antarctic glaciation, the Circum-Antarctic Ocean, and their impact on global paleoceanography: Journal of Geophysical Research: Oceans and Atmospheres, v. 82, p. 3843–3860, https://doi.org/10.1029/JC082i027p03843.

Kim, S., et al., 2018, Seismic stratigraphy of the Central Basin in northwestern Ross Sea slope and rise, Antarctica: Clues to the late Cenozoic ice-sheet dynamics and bottom-current activity: Marine Geology, v. 395, p. 363–379, https://doi.org/10.1016/j.margeo.2017.10.013.

Kominz, M.A., Browning, J.V., Miller, K.G., Sugarman, P.J., Mizintseva, S., and Scotese, C.R., 2008, Late Cretaceous to Miocene sea-level estimates from the New Jersey and Delaware coastal plain coreholes: An error analysis: Basin Research, v. 20, p. 211–226, https://doi.org/10.1111/j.1365-2117.2008.00354.x.

Krissek, L., Browne, G., Carter, L., Cowan, E., Dunbar, G., McKay, R., Naish, T., Powell, R., Reed, J., and Wilch, T., 2007, Sedimentology and stratigraphy of the AND-1B core, ANDRILL McMurdo Ice Shelf Project, Antarctica: Terra Antarctica, v. 14, p. 185–222.

Kulhanek, D.K., et al., 2019, Revised chronostratigraphy of DSDP Site 270 and late Oligocene to early Miocene paleoecology of the Ross Sea sector of Antarctica: Global and Planetary Change, v. 178, p. 46–64, https://doi.org/10.1016/j.gloplacha.2019.04.002.

Laberg, J.S., Eilertsen, R.S., and Vorren, T.O., 2009, The paleo–ice stream in Vestfjorden, north Norway, over the last 35 k.y.: Glacial erosion and sediment yield: Geological Society of America Bulletin, v. 121, p. 434–447, https://doi.org/10.1130/B26277.1.

Laberg, J.S., Eilertsen, R.S., and Salomonsen, G.R., 2018, Deglacial dynamics of the Vestfjorden—Trænadjupet palaeo-ice stream, northern Norway: Boreas, v. 47, p. 225–237, https://doi.org/10.1111/bor.12261.

Leckie, R.M., and Webb, P.-N., 1983, Late Oligocene–early Miocene glacial record of the Ross Sea, Antarctica: Evidence from DSDP Site 270: Geology, v. 11, p. 578–582, https://doi.org/10.1130/0091-7613(1983)11<578:LOMGRO>2.0.CO;2.

Levy, R., et al., 2016, Antarctic Ice Sheet sensitivity to atmospheric CO_2 variations in the early to mid-Miocene: Proceedings of the National Academy of Sciences of the United States of America, v. 113, p. 3453–3458, https://doi.org/10.1073/pnas.1516030113.

Levy, R.H., et al., 2019, Antarctic ice-sheet sensitivity to obliquity forcing enhanced through ocean connections: Nature Geoscience, v. 12, p. 132–137, https://doi.org/10.1038/s41561-018-0284-4.

Lewis, A.R., and Ashworth, A., 2016, An early to middle Miocene record of ice-sheet and landscape evolution from the Friis Hills, Antarctica: Geological Society of America Bulletin, v. 128, p. 719–738, https://doi.org/10.1130/B31319.1.

Lewis, A.R., Marchant, D.R., Kowalewski, D.E., Baldwin, S.L., and Webb, L.E., 2006, The age and origin of the Labyrinth, western Dry Valleys, Antarctica: Evidence for extensive middle Miocene subglacial floods and freshwater discharge to the Southern Ocean: Geology, v. 34, p. 513–516, https://doi.org/10.1130/G22145.1.

Lewis, A.R., Marchant, D.R., Ashworth, A.C., Hemming, S.R., and Machlus, M.L., 2007, Major middle Miocene global climate change: Evidence from East Antarctica and the Transantarctic Mountains: Geological Society of America Bulletin, v. 119, p. 1449–1461, https://doi.org/10.1130/0016-7606(2007)119[1449:MMMGCC]2.0.CO;2.

Lewis, A.R., et al., 2008, Mid-Miocene cooling and the extinction of tundra in continental Antarctica: Proceedings of the National Academy of Sciences of the United States of America, v. 105, p. 10,676–10,680, https://doi.org/10.1073/pnas.0802501105.

Luyendyk, B.P., Sorlien, C.C., Wilson, D.S., Bartek, L.R., and Siddoway, C.S., 2001, Structural and tectonic evolution of the Ross Sea rift in the Cape Colbeck region, Eastern Ross Sea, Antarctica: Tectonics, v. 20, p. 933–958, https://doi.org/10.1029/2000TC001260.

Marschalek, J.W., et al., 2021, A large West Antarctic Ice Sheet explains early Neogene sea-level amplitude: Nature, v. 600, p. 450–455, https://doi.org/10.1038/s41586-021-04148-0.

McCarroll, D., and Rijsdijk, K.F., 2003, Deformation styles as a key for interpreting glacial depositional environments: Journal of Quaternary Science, v. 18, p. 473–489, https://doi.org/10.1002/jqs.780.

McCave, I.N., Manighetti, B., and Robinson, S.G., 1995, Sortable silt and fine sediment size/composition slicing: Parameters for palaeocurrent speed and palaeoceanography: Paleoceanography, v. 10, p. 593–610, https://doi.org/10.1029/94PA03039.

McKay, R., et al., 2009, The stratigraphic signature of the late Cenozoic Antarctic Ice Sheets in the Ross Embayment: Geological Society of America Bulletin, v. 121, p. 1537–1561, https://doi.org/10.1130/B26540.1.

McKay, R., et al., 2012a, Antarctic and Southern Ocean influences on late Pliocene global cooling: Proceedings of the National Academy of Sciences of the United States of America, v. 109, p. 6423–6428, https://doi.org/10.1073/pnas.1112248109.

McKay, R., et al., 2012b, Pleistocene variability of Antarctic Ice Sheet extent in the Ross Embayment: Quaternary Science Reviews, v. 34, p. 93–112, https://doi.org/10.1016/j.quascirev.2011.12.012.

McKay, R., et al., 2022a, A comparison of methods for identifying and quantifying ice rafted debris on the Antarctic margin: Paleoceanography and Paleoclimatology, v. 37, https://doi.org/10.1029/2021PA004404.

McKay, R.M., De Santis, L., Kulhanek, D.K., and Expedition, I.O.D.P., 374 Science Team, 2019, Ross Sea West Antarctic Ice Sheet History: Proceedings of the International Ocean Discovery Program, Volume 374: College Station, Texas, International Ocean Discovery Program, https://doi.org/10.14379/iodp.proc.374.2019.

McKay, R.M., et al., 2022b, Chapter 3—Cenozoic history of Antarctic glaciation and climate from onshore and offshore studies, *in* Florindo, F., Siegert, M., Santis, L.D., and Naish, T., eds., Antarctic Climate Evolution (2nd edition): Amsterdam, Elsevier, p. 41–164, https://doi.org/10.1016/B978-0-12-819109-5.00008-6.

Miller, K.G., Wright, J.D., and Fairbanks, R.G., 1991, Unlocking the Ice House: Oligocene-Miocene oxygen isotopes, eustasy, and margin erosion: Journal of Geophysical Research: Solid Earth, v. 96, p. 6829–6848, https://doi.org/10.1029/90JB02015.

Miller, K.G., Browning, J.V., Schmelz, W.J., Kopp, R.E., Mountain, G.S., and Wright, J.D., 2020, Cenozoic sea-level and cryospheric evolution from deep-sea geochemical and continental margin records: Science Advances, v. 6, https://doi.org/10.1126/sciadv.aaz1346.

Mills, P.C., 1983, Genesis and diagnostic value of soft-sediment deformation structures—A review: Sedimentary Geology, v. 35, p. 83–104, https://doi.org/10.1016/0037-0738(83)90046-5.

Mudelsee, M., Bickert, T., Lear, C.H., and Lohmann, G., 2014, Cenozoic climate changes: A review based on time series analysis of marine benthic $\delta^{18}O$ records: Reviews of Geophysics, v. 52, p. 333–374, https://doi.org/10.1002/2013RG000440.

Naish, T., et al., 2009, Obliquity-paced Pliocene West Antarctic Ice Sheet oscillations: Nature, v. 458, p. 322–328, https://doi.org/10.1038/nature07867.

Naish, T.R., et al., 2001a, Orbitally induced oscillations in the East Antarctic Ice Sheet at the Oligocene/Miocene boundary: Nature, v. 413, p. 719–723, https://doi.org/10.1038/35099534.

Naish, T.R., Barrett, P.J., Dunbar, G.B., Woolfe, K.J., Dunn, A.G., Henrys, S.A., Claps, M., Powell, R.D., and Fielding, C.R., 2001b, Sedimentary cyclicity in CRP drillcore, Victoria Land Basin, Antarctica: Terra Antarctica, v. 8, p. 225–244.

Naish, T.R., Wilson, G.S., Dunbar, G.B., and Barrett, P.J., 2008, Constraining the amplitude of late Oligocene bathymetric changes in western Ross Sea during orbitally-induced oscillations in the East Antarctic Ice Sheet: (2) Implications for global sea-level changes: Palaeogeography, Palaeoclimatology, Palaeoecology, v. 260, p. 66–76, https://doi.org/10.1016/j.palaeo.2007.08.021.

Naish, T.R., Duncan, B., Levy, R., McKay, R.M., Escutia, C., De Santis, L., Colleoni, F., Gasson, E.G.W., DeConto, R.M., and Wilson, G., 2022, Chapter 8—Antarctic Ice Sheet dynamics during the late Oligocene and early Miocene: Climatic conundrums revisited, *in* Florindo, F., Siegert, M., Santis, L.D., and Naish, T., eds., Antarctic Climate Evolution (2nd edition): Amsterdam, Elsevier, p. 363–387, https://doi.org/10.1016/B978-0-12-819109-5.00013-X.

Ó Cofaigh, C., 1996, Tunnel valley genesis: Progress in Physical Geography, v. 20, p. 1–19, https://doi.org/10.1177/030913339602000101.

Ó Cofaigh, C., Dowdeswell, J.A., and Grobe, H., 2001, Holocene glacimarine sedimentation, inner Scoresby Sund, East Greenland: The influence of fast-flowing ice-sheet outlet glaciers: Marine Geology, v. 175, p. 103–129, https://doi.org/10.1016/S0025-3227(01)00117-7.

Ó Cofaigh, C., Andrews, J.T., Jennings, A.E., Dowdeswell, J.A., Hogan, K.A., Kilfeather, A.A., and Sheldon, C., 2013, Glacimarine lithofacies, provenance and depositional processes on a West Greenland trough-mouth fan: Journal of Quaternary Science, v. 28, p. 13–26, https://doi.org/10.1002/jqs.2569.

Ogg, J.G., 2020, Chapter 5—Geomagnetic polarity time scale, *in* Gradstein, F.M., Ogg, J.G., Schmitz, M.D., and Ogg, G.M., eds., Geologic Time Scale 2020:

Elsevier, p. 159–192, https://doi.org/10.1016/B978-0-12-824360-2.00005-X

Ogg, J.G., Ogg, G.M., and Gradstein, F.M., 2016, A Concise Geologic Time Scale: 2016: Elsevier.

Pälike, H., Norris, R.D., Herrle, J.O., Wilson, P.A., Coxall, H.K., Lear, C.H., Shackleton, N.J., Tripati, A.K., and Wade, B.S., 2006, The heartbeat of the Oligocene climate system: Science, v. 314, p. 1894–1898, https://doi.org/10.1126/science.1133822.

Paolo, F.S., Fricker, H.A., and Padman, L., 2015, Volume loss from Antarctic ice shelves is accelerating: Science, v. 348, p. 327–331, https://doi.org/10.1126/science.aaa0940.

Passchier, S., Browne, G., Field, B., Fielding, C.R., Krissek, L.A., Panter, K., Pekar, S.F., and ANDRILL-SMS Science Team, 2011, Early and middle Miocene Antarctic glacial history from the sedimentary facies distribution in the AND-2A drill hole, Ross Sea, Antarctica: Geological Society of America Bulletin, v. 123, p. 2352–2365, https://doi.org/10.1130/B30334.1.

Paxman, G.J.G., Jamieson, S.S.R., Hochmuth, K., Gohl, K., Bentley, M.J., Leitchenkov, G., and Ferraccioli, F., 2019, Reconstructions of Antarctic topography since the Eocene–Oligocene boundary: Palaeogeography, Palaeoclimatology, Palaeoecology, v. 535, https://doi.org/10.1016/j.palaeo.2019.109346.

Paxman, G.J.G., Gasson, E.G.W., Jamieson, S.S.R., Bentley, M.J., and Ferraccioli, F., 2020, Long-term increase in Antarctic Ice Sheet vulnerability driven by bed topography evolution: Geophysical Research Letters, v. 47, https://doi.org/10.1029/2020GL090003.

Pekar, S.F., and DeConto, R.M., 2006, High-resolution ice-volume estimates for the early Miocene: Evidence for a dynamic ice sheet in Antarctica: Palaeogeography, Palaeoclimatology, Palaeoecology, v. 231, p. 101–109, https://doi.org/10.1016/j.palaeo.2005.07.027.

Pekar, S.F., DeConto, R.M., and Harwood, D.M., 2006, Resolving a late Oligocene conundrum: Deep-sea warming and Antarctic glaciation: Palaeogeography, Palaeoclimatology, Palaeoecology, v. 231, p. 29–40, https://doi.org/10.1016/j.palaeo.2005.07.024.

Pérez, L.F., et al., 2022a, Early and middle Miocene ice sheet dynamics in the Ross Sea: Results from integrated core-log-seismic interpretation: Geological Society of America Bulletin, v. 134, p. 348–370, https://doi.org/10.1130/B35814.1.

Pérez, L.F., et al., 2022b, Early to middle Miocene ice sheet dynamics in the westernmost Ross Sea (Antarctica): Regional correlations: Global and Planetary Change, v. 216, https://doi.org/10.1016/j.gloplacha.2022.103891.

Pollard, D., and DeConto, R.M., 2009, Modelling West Antarctic Ice Sheet growth and collapse through the past five million years: Nature, v. 458, p. 329–332, https://doi.org/10.1038/nature07809.

Powell, R.D., and Cooper, J.M., 2002, A glacial sequence stratigraphic model for temperate, glaciated continental shelves, *in* Dowdeswell, J.A., and Ó Cofaigh, C., eds., Glacier-Influenced Sedimentation on High-Latitude Continental Margins: Geological Society, London, Special Publication 203, p. 215–244, https://doi.org/10.1144/GSL.SP.2002.203.01.12.

Powell, R.D., and Domack, E., 1995, Modern glaciomarine environments: Modern Glacial Environments, v. 1, p. 445–486.

Powell, R.D., and Molnia, B.F., 1989, Glacimarine sedimentary processes, facies and morphology of the south-southeast Alaska shelf and fjords: Marine Geology, v. 85, p. 359–390, https://doi.org/10.1016/0025-3227(89)90160-6.

Powell, R.D., Laird, M.G., Naish, T.R., Fielding, C.R., Krissek, L.A., and van der Meer, J.J.M., 2001, Depositional environments for strata cored in CRP-3 (Cape Roberts Project), Victoria Land Basin, Antarctica: Palaeoglaciological and palaeoclimatological inferences: Terra Antarctica, v. 8, p. 207–216.

Pritchard, H.D., Ligtenberg, S.R.M., Fricker, H.A., Vaughan, D.G., van den Broeke, M.R., and Padman, L., 2012, Antarctic ice loss driven by ice-shelf melt: Nature, v. 484, p. 502–505, https://doi.org/10.1038/nature10968.

Prothro, L.O., Simkins, L.M., Majewski, W., and Anderson, J.B., 2018, Glacial retreat patterns and processes determined from integrated sedimentology and geomorphology records: Marine Geology, v. 395, p. 104–119, https://doi.org/10.1016/j.margeo.2017.09.012.

Prothro, L.O., Majewski, W., Yokoyama, Y., Simkins, L.M., Anderson, J.B., Yamane, M., Miyairi, Y., and Ohkouchi, N., 2020, Timing and pathways of East Antarctic Ice Sheet retreat: Quaternary Science Reviews, v. 230, https://doi.org/10.1016/j.quascirev.2020.106166.

Rae, J.W.B., Zhang, Y.G., Liu, X., Foster, G.L., Stoll, H.M., and Whiteford, R.D.M., 2021, Atmospheric CO_2 over the past 66 million years from marine archives: Annual Review of Earth and Planetary Sciences, v. 49, p. 609–641, https://doi.org/10.1146/annurev-earth-082420-063026.

Rebesco, M., Hernández-Molina, F.J., Van Rooij, D., and Wåhlin, A., 2014, Contourites and associated sediments controlled by deep-water circulation processes: State-of-the-art and future considerations: Marine Geology, v. 352, p. 111–154, https://doi.org/10.1016/j.margeo.2014.03.011.

Rignot, E., Jacobs, S., Mouginot, J., and Scheuchl, B., 2013, Ice-shelf melting around Antarctica: Science, v. 341, p. 266–270, https://doi.org/10.1126/science.1235798.

Rosenblume, J.A., and Powell, R.D., 2019, Glacial sequence stratigraphy of ANDRILL-1B core reveals a dynamic subpolar Antarctic Ice Sheet in Ross Sea during the late Miocene: Sedimentology, v. 66, p. 2072–2097, https://doi.org/10.1111/sed.12592.

Salvi, C., Busetti, M., Marinoni, L., and Brambati, A., 2006, Late Quaternary glacial marine to marine sedimentation in the Pennell Trough (Ross Sea, Antarctica): Palaeogeography, Palaeoclimatology, Palaeoecology, v. 231, p. 199–214, https://doi.org/10.1016/j.palaeo.2005.07.034.

Sangiorgi, F., et al., 2018, Southern Ocean warming and Wilkes Land ice sheet retreat during the mid-Miocene: Nature Communications, v. 9, 317, https://doi.org/10.1038/s41467-017-02609-7.

Shevenell, A.E., Kennett, J.P., and Lea, D.W., 2004, Middle Miocene Southern Ocean cooling and Antarctic cryosphere expansion: Science, v. 305, p. 1766–1770, https://doi.org/10.1126/science.1100061.

Shevenell, A.E., Kennett, J.P., and Lea, D.W., 2008, Middle Miocene ice sheet dynamics, deep-sea temperatures, and carbon cycling: A Southern Ocean perspective: Geochemistry, Geophysics, Geosystems, v. 9, https://doi.org/10.1029/2007GC001736.

Simkins, L.M., Anderson, J.B., Greenwood, S.L., Gonnermann, H.M., Prothro, L.O., Halberstadt, A.R.W., Stearns, L.A., Pollard, D., and DeConto, R.M., 2017, Anatomy of a meltwater drainage system beneath the ancestral East Antarctic Ice Sheet: Nature Geoscience, v. 10, p. 691–697, https://doi.org/10.1038/ngeo3012.

Smith, E.C., et al., 2020, Detailed seismic bathymetry beneath Ekström Ice Shelf, Antarctica: Implications for glacial history and ice-ocean interaction: Geophysical Research Letters, v. 47, https://doi.org/10.1029/2019GL086187.

Smith, J.A., Graham, A.G.C., Post, A.L., Hillenbrand, C.-D., Bart, P.J., and Powell, R.D., 2019, The marine geological imprint of Antarctic ice shelves: Nature Communications, v. 10, 5635, https://doi.org/10.1038/s41467-019-13496-5.

Sorlien, C.C., Luyendyk, B.P., Wilson, D.S., Decesari, R.C., Bartek, L.R., and Diebold, J.B., 2007, Oligocene development of the West Antarctic Ice Sheet recorded in eastern Ross Sea strata: Geology, v. 35, p. 467–470, https://doi.org/10.1130/G23387A.1.

Sosdian, S.M., Greenop, R., Hain, M.P., Foster, G.L., Pearson, P.N., and Lear, C.H., 2018, Constraining the evolution of Neogene ocean carbonate chemistry using the boron isotope pH proxy: Earth and Planetary Science Letters, v. 498, p. 362–376, https://doi.org/10.1016/j.epsl.2018.06.017.

Sperazza, M., Moore, J.N., and Hendrix, M.S., 2004, High-resolution particle size analysis of naturally occurring very fine-grained sediment through laser diffractometry: Journal of Sedimentary Research, v. 74, p. 736–743, https://doi.org/10.1306/031104740736.

Steinthorsdottir, M., et al., 2021, The Miocene: The future of the past: Paleoceanography and Paleoclimatology, v. 36, https://doi.org/10.1029/2020PA004037.

Sugden, D., and Denton, G., 2004, Cenozoic landscape evolution of the Convoy Range to Mackay Glacier area, Transantarctic Mountains: Onshore to offshore synthesis: Geological Society of America Bulletin, v. 116, p. 840–857, https://doi.org/10.1130/B25356.1.

Super, J.R., Thomas, E., Pagani, M., Huber, M., O'Brien, C., and Hull, P.M., 2018, North Atlantic temperature and pCO_2 coupling in the early-middle Miocene: Geology, v. 46, p. 519–522, https://doi.org/10.1130/G40228.1.

Vaughan, D.G., et al., 2013, Observations: Cryosphere, *in* Stocker, T.F., et al., eds., Climate Change 2013: The Physical Science Basis: Contribution of Working Group I to the Fifth Assessment Report of the Intergovernmental Panel on Climate Change: Cambridge, UK, Cambridge University Press, p. 317–382.

Warny, S., Askin, R.A., Hannah, M.J., Mohr, B.A.R., Raine, J.I., Harwood, D.M., and Florindo, F., and the SMS Science Team, 2009, Palynomorphs from a sediment core reveal a sudden remarkably warm Antarctica during the middle Miocene: Geology, v. 37, p. 955–958, https://doi.org/10.1130/G30139A.1.

Whitehead, J.M., Harwood, D.M., McKelvey, B.C., Hambrey, M.J., and McMinn, A., 2004, Diatom biostratigraphy of the Cenozoic glaciomarine Pagodroma Group, northern Prince Charles Mountains, East Antarctica: Australian Journal of Earth Sciences, v. 51, p. 521–547, https://doi.org/10.1111/j.1400-0952.2004.01072.x.

Wilson, D.S., and Luyendyk, B.P., 2009, West Antarctic paleotopography estimated at the Eocene-Oligocene climate transition: Geophysical Research Letters, v. 36, https://doi.org/10.1029/2009GL039297.

Wilson, D.S., Pollard, D., DeConto, R.M., Jamieson, S.S.R., and Luyendyk, B.P., 2013, Initiation of the West Antarctic Ice Sheet and estimates of total Antarctic ice volume in the earliest Oligocene: Geophysical Research Letters, v. 40, p. 4305–4309, https://doi.org/10.1002/grl.50797.

Wright, J.D., Miller, K.G., and Fairbanks, R.G., 1992, Early and Middle Miocene stable isotopes: Implications for Deepwater circulation and climate: Paleoceanography, v. 7, p. 357–389, https://doi.org/10.1029/92PA00760.

You, Y., Huber, M., Müller, R.D., Poulsen, C.J., and Ribbe, J., 2009, Simulation of the Middle Miocene Climate Optimum: Geophysical Research Letters, v. 36, https://doi.org/10.1029/2008GL036571.

Zachos, J.C., Breza, J.R., and Wise, S.W., 1992, Early Oligocene ice-sheet expansion on Antarctica: Stable isotope and sedimentological evidence from Kerguelen Plateau, southern Indian Ocean: Geology, v. 20, p. 569–573, https://doi.org/10.1130/0091-7613(1992)020<0569:EOISEO>2.3.CO;2.

Zachos, J.C., Flower, B.P., and Paul, H., 1997, Orbitally paced climate oscillations across the Oligocene/Miocene boundary: Nature, v. 388, p. 567–570, https://doi.org/10.1038/41528.

Zachos, J.C., Pagani, M., Sloan, L., Thomas, E., and Billups, K., 2001, Trends, rhythms, and aberrations in global climate 65 Ma to present: Science, v. 292, p. 686–693, https://doi.org/10.1126/science.1059412.

Zurli, L., Perotti, M., and Talarico, F.M., 2022, Data report: Petrology of gravel-sized clasts from Site U1521 core, IODP Expedition 374, Ross Sea West Antarctic Ice Sheet History: Proceedings of the International Ocean Discovery Program, Volume 374, https://doi.org/10.14379/iodp.proc.374.201.2022

Science Editor: Troy Rasbury
Associate Editor: Zoltan Sylvester

Manuscript Received 14 February 2024
Revised Manuscript Received 6 August 2024
Manuscript Accepted 6 September 2024